2020

A kirigami approach for controlling mechanical and sensing properties of films

Dohgyu Hwang
Iowa State University

A kirigami approach for controlling mechanical and sensing properties of films

by

Dohgyu Hwang

A thesis submitted to the graduate faculty

in partial fulfillment of the requirements for the degree of

MASTER OF SCIENCE

Major: Materials Science and Engineering

Program of Study Committee:
Michael D. Bartlett, Major Professor
Jaeyoun Kim
Peter C. Collins

The student author, whose presentation of the scholarship herein was approved by the program of study committee, is solely responsible for the content of this thesis. The Graduate College will ensure this thesis is globally accessible and will not permit alterations after a degree is conferred.

Iowa State University

Ames, Iowa

2020

TABLE OF CONTENTS

Page

LIST OF TABLES

Page

LIST OF FIGURES

Page

ACKNOWLEDGMENTS

I express my deepest gratitude to my advisor, Professor Michael Bartlett. I am grateful that Mike offered me the opportunity to work with him 4 years ago. Mike is the best advisor a student can ever hope for. He possesses the rare combination of extensive scientific knowledge while also showing care and concern for others. He has taught me the beauty of science and how it applies to the real world. Whenever I am working on a project and I bring him new results with excitement, he shows great enthusiasm and provide insightful feedback with passion to help me make it better. I was struggling in the beginning of my graduate program but through his sincere concern, guidance and going the extra mile to address my issues, I was able to overcome the challenges I faced. I am sincerely looking forward to continuously working with him for the next few years at Virginia Tech.

Diana, I cannot thank you enough for everything you have done for me, especially during the challenging moments in my life. You taught me numerous invaluable life lessons that I take to heart. You transformed me into a completely different person through consistent acts of courage daily. You truly taught me to be myself, to learn my values and to influence people in a favorable light. You basically turned me into a better version of me. Gene, Chase, Nickie, Jacob, and Jinho our close friendship brought joy to my life. Your friendship showed me how you care for someone you appreciate. Even though I will be leaving Ames, I will keep in touch and still help with your Korean classes and hang out.

Lastly, I would like to thank my beloved parents, Ye-seo Kwon and Ji-baek Hwang, who patiently waited for me to realize what I genuinely want in my life. They provided me with unwavering and unconditional support, allowing me to follow my dreams of becoming an engineer on the other side of the world. I also want to thank my supportive siblings, Rae-gyo Hwang, and Jeong-hyeon Hwang, who have stood by me no matter how many times we fought growing up. Without my family's support and encouragement, I would not be where I am today.

ABSTRACT

Tuning the layout of elasticity in materials opens new opportunities to add various functionalities into a system, ranging from load-enduring capacity and shape-morphing capability in aeronautics to self-foldability and controlled diffusion rates in drug delivery applications. Recently, the Japanese art of paper cutting technique called *kirigami* has positioned itself as a simple yet powerful strategy to program unique functionalities into intrinsically inextensible, stiff materials without adjusting chemical compositions, including elastic softening, creation of complex 3D structures, and extreme stretchability. Thus, various applications have been realized by utilizing the kirigami principle. These applications include wearable electronics, sensors, stretchable lithium batteries, solar trackers, and reconfigurable structures. However, coupling the primary geometric deformation modes (*i.e.*, bending and rotation) in kirigami films to control mechanical response as well as electronic properties (*e.g.*, shift in resonant frequency) have been limited. In this thesis, we present a strategy where the inclusion of carefully designed cuts allows for fine tuning of mechanical and electronic properties of materials.

Starting from fundamentals of kirigami mechanics, we show that stiffness tunability and deformability of kirigami structures are significantly influenced by the addition of minor cuts adjacent to major cuts. The dimension and position of minor cuts relative to major cuts determines geometric deformation modes between bending of beams and hinge rotations, which results in high tunability of mechanical properties. The experimental results are validated by beam mechanics with different boundary conditions (Chapter 2). The sensors for human activity monitoring and soft robotic systems require considerable extents of deformation. Furthermore, reducing or eliminating wiring components allows for more compliant and less complex systems by excluding semirigid wiring or connection points. We create a kirigami-inspired passive resonant sensor where the deformation normal to the planar surface changes the capacitance, inductance, and resonant frequency. This

study demonstrates that the device allows for accurate measurements of large deformations ($>$ 10X sensor thickness) in both air and water media (Chapter 3).

CHAPTER 1. GENERAL INTRODUCTION

1.1 Overview

Programming elasticity into targeted areas of materials provides new opportunities for adding multi-functionality into a system, ranging from load-bearing capacity and rapid-morphing capability in aeronautics Faber et al. (2018) to self-foldability and chemical diffusion rates in drug delivery applications Fernandes and Gracias (2012). The fabrication strategy is also utilized in other emerging and developed fields, such as stretchable electronics, soft robotics, and biomedical engineering Callens and Zadpoor (2018); van Manen et al. (2018); Bartlett et al. (2015); Kim et al. (2008); Shepherd et al. (2011); Azam et al. (2011); Jenett et al. (2017); Su et al. (2017); Mosadegh et al. (2014). In essence, tailoring the array of elasticity in materials, through thickness or across the surface, realizes two major functionalities: shape-morphability and stiffness-tunability. To date, two different deformation mechanisms, bending and buckling, are present from a mechanical viewpoint to control the above characteristics Tang et al. (2015); Gatt et al. (2015); Cho et al. (2014). Bending occurs when the internal stress induced over a cross-section of a structure by moments is non-uniform. Buckling occurs when compressive stresses above a critical point act over a structure Gere and Timoshenko (1997). Material or structural gradients that induce non-uniform stress and deformations have been introduced in various dimensionalities (*i.e.*, positional, linear, areal, volumetric) by using fast-growing 3D additive manufacturing processes and other techniques such as assembly through transfer printing of diverse components Kokkinis et al. (2018). By tuning material properties the shape-shifting and stiffness-tuning abilities can be dynamically controlled in response to various environmental conditions, such as temperature, light, pH, electromagnetism or humidity Van Manen et al. (2017); So and Hayward (2017); Baker et al. (2016); Kim et al. (2018). Furthermore, by tuning geometric parameters without changing chemical compositions, the programmed system can also exhibit similar effects. However, the limited choice of materials available

for 3D printing and complex fabrication processes pose challenges in developing multi-functional programmable materials.

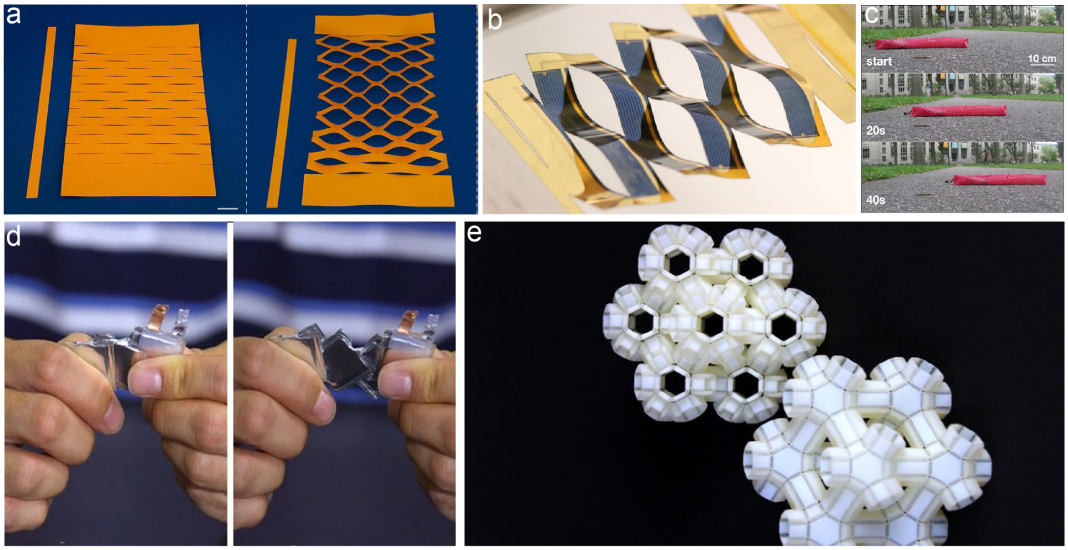

Figure 1.1 : (a) original and deformed patterned sheets Callens and Zadpoor (2018). Reproduced with permission. Copyright 2018, Elsevier (b) kirigami-inspired solar cells to enhance solar light absorption Lamoureux et al. (2015). Reproduced with permission. Copyright 2015, Springer Nature (c) snake robot that moves with frictional interaction of patterned skin Rafsanjani et al. (2018). Reproduced with permission. Copyright 2018, AAAS (d) stretchable lithium batteries Song et al. (2015). Reproduced with permission. Copyright 2015, Springer Nature (e) reconfigurable structures Overvelde et al. (2017).Reproduced with permission. Copyright 2017, Springer Nature

In recent years, the Japanese art of paper cutting called "*kirigami*", which is a simple subtractive approach, has emerged as a promising research tool for imparting unique functionalities into intrinsically stiff materials without tuning chemical compositions, such as extreme extensibility, formation of complex 3D morphologies, and elastic softening.Blees et al. (2015); Virk et al. (2013); Castle et al. (2016); Neville et al. (2016); Hanakata et al. (2016); Liu et al. (2017); Sussman et al. (2015) Therefore, various applications have been developed by exploiting the kirigami principle. These applications include solar trackers, stretchable lithium batteries, wearable electronics, soft robots, bandages, sensors, and reconfigurable structures (See Figure 1.1) Rafsanjani and Bertoldi

(2017); Lamoureux et al. (2015); Rafsanjani et al. (2018); Song et al. (2015); Overvelde et al. (2017); Celli et al. (2018); Iwata and Iwase (2017); Yamamoto et al. (2016); Guo et al. (2016); Lee et al. (2017); Firouzeh and Paik (2015); Sareh and Rossiter (2013); Wang et al. (2017). The governing mechanics of deformation and architecture of the kirigami patterned system under external stimuli are different from those of pristine materials. Kirigami principles generate geometric deformations induced by the array and dimensions of prescribed cuts rather than intrinsic material elasticity. In contrast, properties and structures of pristine materials are dominated by atomic and molecular interactions.

However, several critical research problems in this area persist. Although two major geometric deformation modes in kirigami structures (*e.g.*, bending and rotation) were previously explored, the synergistic coupling of the two deformation modes has not been studied Isobe and Okumura (2016); Shyu et al. (2015); Rafsanjani and Bertoldi (2017); Cho et al. (2014); Tang et al. (2016); Gatt et al. (2015); Tang et al. (2015). In addition, most demonstrations on wireless kirigami/origami antennas stop short of exploring the structures to report the relationship between the resonant scattering parameters and the extent of deformations Liu et al. (2014); Fu et al. (2018); Liu et al. (2015).

The goal of this research is to develop a fundamental understanding of how kirigami structures can create spatial layouts of elasticity to control mechanical and functional response such as electrical properties. Specifically, what is the design approach that determines the deformation modes of kirigami structures? How would the structural deformation modulate electrical properties for strain monitoring applications?

This thesis comprises four sections: an introduction, two experimental sections, and a final chapter discussing conclusions, contributions, and outlooks. We begin from understanding the kirigami designs that determine two deformation modes between bending of beams and rotation of hinges Hwang and Bartlett (2018). This is achieved by the position and dimension of minor cuts adjacent to major cuts. (Chapter 2) We further extend the utility of the kirigami principle to tuning electrical properties Charkhabi et al. (2019). we create the kirigami antenna to investigate the relationship between the extension length and the resonant scattering parameters both in the

air and water media. The out-of-plane deformation of the spiral design affects the capacitance and the inductance, which is utlized for measuring the water flow rate in the demonstration. (Chapter 3) Finally, we conclude this manuscript with comprehensive discussion of the kirigami approach that affects mechanical and sensing responses. (Chapter 4)

1.2 Fundamentals of Kirigami Mechanics

Kirigami engineering mechanics, depending on designs, lies in the combination of instability-induced deformation of slender beams which are defined by long parallel cuts and of hinges that connect networks of stiff islands. We will primarily review the deformation of slender beams, as the deformation of hinges follow a similar set of mechanics. Mechanical characteristics, softness and resulting morphologies, are governed by geometric parameters (length l, width w, thickness t), material elasticity (E), and loading conditions (*e.g.*, direction, boundary conditions).

Consider a slender beam ($l/t \gg 1$) that constitutes a 2D kirigami-patterned sheet and deforms under flexural loading, assuming that the beam behaves in a linearly elastic manner and deflections δ are very small ($l \gg \delta$). The strain energy stored in the beam is expressed such that $U_s = \int \frac{M^2}{2EI} dx \backsimeq \frac{Ew^3 t\delta^2}{l^3}$, where M is the bending moment, E is the elastic modulus, and I is the second moment of area. To create 3D configurations from 2D patterned sheets as well as elastic softening under mechanical loading, it is adequate to think that morphing behavior should undergo an instability-induced transition where a new state is energetically more favorable than an initial state under loading. In a basic kirigami design that consists of transverse long prismatic beams, the initial and new state can correspond to in-plane and out-of-plane bending, respectively. Assuming that modulus and length are constant, the variation of in-plane bending strain energy U_i is largely dependent on w^3, whereas the out-of-plane bending strain energy U_o shows a large dependence on t^3. When the two energies equalize under loading, a phase transition induced by mechanical instability occurs.

By simply comparing the two in-plane and out-of-plane energies, we see that $U_o/U_i \sim (t/w)^2$ Holmes (2019). In the thin limit (i.e., for small values of t/w), the quantity is very small, indicating that out-of-plane bending mode is the path for accumulating less strain energy as well as extra elastic softening. In contrast, in relatively thick samples ($t \sim w$), the values of two energies are similar, resulting in suppression of the phase transition.

1.3 Hypothesis

We hypothesize that programming the spatial layout of elasticity based upon kirigami principles will have a significant contribution to material performance, such as mechanical and electrical properties. Specifically, (1) The mechanical properties such as stiffness and ultimate strain will be significantly affected by the inclusion of minor cut structures to conventional major cut structures. (2) The resonant frequency of an antenna will be highly tunable in relation to the large extent of deformations.

1.4 Thesis Organization

This thesis will explore the coupling of the two major deformation modes in kirigami structures, and the relationship between the extent of deformations and the resonant scattering parameters in wireless kirigami antennas.

Chapter 2 begins with discussing the two deformation modes of bending and rotation in kirigami structures individually, and how these deformation modes can be coupled through the addition of minor cuts which results in high tunability of stiffness and ultimate strain. These mechanical properties are explained by analytical expressions based on mechanics of beams with various boundary conditions. This understanding is applied to developing resistance-invariant stretchable conductors and highly deformable magnetoactive kirigami sheets. Chapter 3 exploits kirigami principles to tune resonant scattering parameters as a function of out-of-plane extensions. The antennas demonstrate high deformability, robustness over repetitive extensions, and measuring capacity of the flow rate of liquid in a closed pipe. Chapter 4 summarizes this work and presents future work.

1.5 References

Azam, A., Laflin, K. E., Jamal, M., Fernandes, R., and Gracias, D. H. (2011). Self-folding micropatterned polymeric containers. *Biomedical Microdevices*, 13(1):51–58.

Baker, A. B., Wass, D. F., and Trask, R. S. (2016). 4D sequential actuation: Combining ionoprinting and redox chemistry in hydrogels. *Smart Materials and Structures*, 25(10).

Bartlett, N. W., Tolley, M. T., Overvelde, J. T. B., Weaver, J. C., Mosadegh, B., Bertoldi, K., G. M.Whitesides, and Wood, R. J. (2015). A 3D-printed, functionally graded soft robot powered by combustion. *Science*, 349(6244):161–166.

Blees, M. K., Barnard, A. W., Rose, P. a., Roberts, S. P., McGill, K. L., Huang, P. Y., Ruyack, A. R., Kevek, J. W., Kobrin, B., Muller, D. a., and McEuen, P. L. (2015). Graphene kirigami. *Nature*, 524:204–207.

Callens, S. J. and Zadpoor, A. A. (2018). From flat sheets to curved geometries: Origami and kirigami approaches. *Materials Today*, 21(3):241–264.

Castle, T., Sussman, D. M., Tanis, M., and Kamien, R. D. (2016). Additive lattice kirigami. *Science Advances*, 2(9):e1601258–e1601258.

Celli, P., McMahan, C., Ramirez, B., Bauhofer, A., Naify, C., Hofmann, D., Audoly, B., and Daraio, C. (2018). Shape-morphing architected sheets with non-periodic cut patterns.

Charkhabi, S., Chan, Y. J., Hwang, D.-g., Frey, S. T., Bartlett, M. D., and Reuel, N. F. (2019). Kirigami-Enabled , Passive Resonant Sensors for Wireless Deformation Monitoring. *Advanced Materials Technologies*, 1800683:1–8.

Cho, Y., Shin, J.-H., Costa, A., Kim, T. A., Kunin, V., Li, J., Lee, S. Y., Yang, S., Han, H. N., Choi, I.-S., and Srolovitz, D. J. (2014). Engineering the shape and structure of materials by fractal cut. *Proceedings of the National Academy of Sciences of the United States of America*, 111(49):17390–5.

Faber, J. A., Arrieta, A. F., and Studart, A. R. (2018). Bioinspired spring origami. *Science*, 359(6382):1386–1391.

Fernandes, R. and Gracias, D. H. (2012). Self-folding polymeric containers for encapsulation and delivery of drugs. *Advanced Drug Delivery Reviews*, 64(14):1579–1589.

Firouzeh, A. and Paik, J. (2015). The Design and Modeling of a Novel Resistive Stretch Sensor with Tunable Sensitivity. *IEEE Sensors Journal*, 15(11):6390–6398.

Fu, H., Nan, K., Bai, W., Huang, W., Bai, K., Lu, L., Zhou, C., Liu, Y., Liu, F., Wang, J., Han, M., Yan, Z., Luan, H., Zhang, Y., Zhang, Y., Zhao, J., Cheng, X., Li, M., Lee, J. W., Liu, Y.,

Fang, D., Li, X., Huang, Y., Zhang, Y., and Rogers, J. A. (2018). Morphable 3D mesostructures and microelectronic devices by multistable buckling mechanics. *Nature Materials*, 17(3):268–276.

Gatt, R., Mizzi, L., Azzopardi, J. I., Azzopardi, K. M., Attard, D., Casha, A., Briffa, J., and Grima, J. N. (2015). Hierarchical Auxetic Mechanical Metamaterials. *Scientific Reports*, 5:8395.

Gere, J. M. and Timoshenko, S. P. (1997). *Mechanics of Materials*. PWS Publishing Company, 4th edition.

Guo, H., Yeh, M. H., Lai, Y. C., Zi, Y., Wu, C., Wen, Z., Hu, C., and Wang, Z. L. (2016). All-in-One Shape-Adaptive Self-Charging Power Package for Wearable Electronics. *ACS Nano*, 10(11):10580–10588.

Hanakata, P. Z., Qi, Z., Campbell, D. K., and Park, H. S. (2016). Highly stretchable MoS2 kirigami. *Nanoscale*, 8(1):458–463.

Holmes, D. P. (2019). Elasticity and Stability of Shape Changing Structures. *Current Opinion in Colloid & Interface Science*, 40:118–137.

Hwang, D. G. and Bartlett, M. D. (2018). Tunable Mechanical Metamaterials through Hybrid Kirigami Structures. *Scientific Reports*, 8(1):1–8.

Isobe, M. and Okumura, K. (2016). Initial rigid response and softening transition of highly stretchable kirigami sheet materials. *Scientific Reports*, 6(April):24758.

Iwata, Y. and Iwase, E. (2017). Stress-Free Stretchable Electronic Device. *Micro Electro Mechanical Systems (MEMS)*, 2017 IEEE:231–234.

Jenett, B., Calisch, S., Cellucci, D., Cramer, N., Gershenfeld, N., Swei, S., and Cheung, K. C. (2017). Digital Morphing Wing: Active Wing Shaping Concept Using Composite Lattice-Based Cellular Structures. *Soft Robotics*, 4(1):33–48.

Kim, D.-h., Song, J., Mook, W., Kim, H.-s., Kim, R.-h., Liu, Z., Huang, Y. Y., Hwang, K.-c., Zhang, Y.-w., and Rogers, J. A. (2008). Materials and noncoplanar mesh designs for integrated circuits with linear elastic responses to extreme mechanical deformations. *Proceedings of the National Academy of Sciences of the United States of America*, 105(48):18675–18680.

Kim, Y., Yuk, H., Zhao, R., Chester, S. A., and Zhao, X. (2018). Printing ferromagnetic domains for untethered fast-transforming soft materials. *Nature Letter*, 558:274–279.

Kokkinis, D., Bouville, F., and Studart, A. R. (2018). 3D Printing of Materials with Tunable Failure via Bioinspired Mechanical Gradients. *Advanced Materials*, 1705808:1–9.

Lamoureux, A., Lee, K., Shlian, M., Forrest, S. R., and Shtein, M. (2015). Dynamic kirigami structures for integrated solar tracking. *Nature Communications*, 6:8092.

Lee, Y. K., Jang, K.-I., Ma, Y., Koh, A., Chen, H., Jung, H. N., Kim, Y., Kwak, J. W., Wang, L., Xue, Y., Yang, Y., Tian, W., Jiang, Y., Zhang, Y., Feng, X., Huang, Y., and Rogers, J. A. (2017). Chemical Sensing Systems that Utilize Soft Electronics on Thin Elastomeric Substrates with Open Cellular Designs. *Advanced Functional Materials*, 201605476:1605476.

Liu, X., Yao, S., and Georgakopoulos, S. V. (2015). Reconfigurable origami equiangular conical spiral antenna. *IEEE Antennas and Propagation Society, AP-S International Symposium (Digest)*, 2015-Octob:2263–2264.

Liu, X., Yao, S., Georgakopoulos, S. V., Cook, B. S., and Tentzeris, M. M. (2014). Reconfigurable helical antenna based on an origami structure for wireless communication system. *IEEE MTT-S International Microwave Symposium Digest*, (1):12–15.

Liu, Y., Shaw, B., Dickey, M. D., and Genzer, J. (2017). Sequential self-folding of polymer sheets. *Science Advances*, 3:1–7.

Mosadegh, B., Polygerinos, P., Keplinger, C., Wennstedt, S., Shepherd, R. F., Gupta, U., Shim, J., Bertoldi, K., Walsh, C. J., and Whitesides, G. M. (2014). Pneumatic networks for soft robotics that actuate rapidly. *Advanced Functional Materials*, 24(15):2163–2170.

Neville, R. M., Scarpa, F., and Pirrera, A. (2016). Shape morphing Kirigami mechanical metamaterials. *Scientific Reports*, 6(1):31067.

Overvelde, J. T., Weaver, J. C., Hoberman, C., and Bertoldi, K. (2017). Rational design of reconfigurable prismatic architected materials. *Nature*, 541(7637):347–352.

Rafsanjani, A. and Bertoldi, K. (2017). Buckling-Induced Kirigami. *Physical Review Letters*, 118(8):84301.

Rafsanjani, A., Zhang, Y., Liu, B., Rubinstein, S. M., and Bertoldi, K. (2018). Kirigami skins make a simple soft actuator crawl. *Science Robotics*, 3(15):eaar7555.

Sareh, S. and Rossiter, J. (2013). Kirigami artificial muscles with complex biologically inspired morphologies. *Smart Materials and Structures*, 22(1):014004.

Shepherd, R. F., Ilievski, F., Choi, W., Morin, S. A., Stokes, A. A., Mazzeo, A. D., Chen, X., Wang, M., and Whitesides, G. M. (2011). Multigait soft robot. *Proceedings of the National Academy of Sciences of the United States of America*, 108(51):20400–20403.

Shyu, T. C., Damasceno, P. F., Dodd, P. M., Lamoureux, A., Xu, L., Shlian, M., Shtein, M., Glotzer, S. C., and Kotov, N. A. (2015). A kirigami approach to engineering elasticity in nanocomposites through patterned defects. *Nature Materials*, 14(8):785–789.

So, S. and Hayward, R. C. (2017). Tunable Upper Critical Solution Temperature of Poly(N-isopropylacrylamide) in Ionic Liquids for Sequential and Reversible Self-Folding. *ACS Applied Materials and Interfaces*, 9(18):15785–15790.

Song, Z., Wang, X., Lv, C., An, Y., Liang, M., Ma, T., He, D., Zheng, Y.-J., Huang, S.-Q., Yu, H., and Jiang, H. (2015). Kirigami-based stretchable lithium-ion batteries. *Scientific Reports*, 5:10988.

Su, Y., Ping, X., Yu, K. J., Lee, J. W., Fan, J. A., Wang, B., Li, M., Li, R., Harburg, D. V., Huang, Y. A., Yu, C., Mao, S., Shim, J., Yang, Q., Lee, P. Y., Armonas, A., Choi, K. J., Yang, Y., Paik, U., Chang, T., Dawidczyk, T. J., Huang, Y., Wang, S., and Rogers, J. A. (2017). In-Plane Deformation Mechanics for Highly Stretchable Electronics. *Advanced Materials*, 29(8):1–12.

Sussman, D. M., Cho, Y., Castle, T., Gong, X., Jung, E., Yang, S., and Kamien, R. D. (2015). Algorithmic lattice kirigami: A route to pluripotent materials. *Proceedings of the National Academy of Sciences*, 112(24):7449–7453.

Tang, J., Wang, J., Liu, J., and Zhou, Y. (2016). Jumping liquid metal droplet in electrolyte triggered by solid metal particles. *Applied Physics Letters*, 108(22):223901.

Tang, Y., Lin, G., Han, L., Qiu, S., Yang, S., and Yin, J. (2015). Design of Hierarchically Cut Hinges for Highly Stretchable and Reconfigurable Metamaterials with Enhanced Strength. *Advanced Materials*, 27(44):7181–7190.

Van Manen, T., Janbaz, S., and Zadpoor, A. A. (2017). Programming 2D/3D shape-shifting with hobbyist 3D printers. *Materials Horizons*, 4(6):1064–1069.

van Manen, T., Janbaz, S., and Zadpoor, A. A. (2018). Programming the shape-shifting of flat soft matter. *Materials Today*, 21(2):144–163.

Virk, K., Monti, a., Trehard, T., Marsh, M., Hazra, K., Boba, K., Remillat, C. D. L., Scarpa, F., and Farrow, I. R. (2013). SILICOMB PEEK Kirigami cellular structures: mechanical response and energy dissipation through zero and negative stiffness. *Smart Materials and Structures*, 22(8):084014.

Wang, W., Li, C., Rodrigue, H., Yuan, F., Han, M. W., Cho, M., and Ahn, S. H. (2017). Kirigami/Origami-Based Soft Deployable Reflector for Optical Beam Steering. *Advanced Functional Materials*, 27(7):1604214.

Yamamoto, Y., Harada, S., Yamamoto, D., Honda, W., Arie, T., Akita, S., and Takei, K. (2016). Printed multifunctional flexible device with an integrated motion sensor for health care monitoring. *Science Advances*, 2(11):e1601473–e1601473.

CHAPTER 2. TUNABLE MECHANICAL METAMATERIALS THROUGH HYBRID KIRIGAMI STRUCTURES

Doh-Gyu Hwang, Michael D. Bartlett

Department of Materials Science and Engineering, Soft Materials and Structures Lab, Iowa State University of Science and Technology, 528 Bissell Rd, Ames, IA, 50011, USA

Modified from a manuscript published in *Scientific Reports*

2.1 Abstract

Inspired by the art of paper cutting, kirigami provides intriguing tools to create materials with unconventional mechanical and morphological responses. This behavior is appealing in multiple applications such as stretchable electronics and soft robotics and presents a tractable platform to study structure-property relationships in material systems. However, mechanical response is typically controlled through a single or fractal cut type patterned across an entire kirigami sheet, limiting deformation modes and tunability. Here we show how hybrid patterns of major and minor cuts creates new opportunities to introduce boundary conditions and non-prismatic beams to enable highly tunable mechanical responses. This hybrid approach reduces stiffness by a factor of $\sim$ 30 while increasing ultimate strain by a factor of 2 (up to 750 % strain) relative to single incision patterns. We present analytical models and generate general design criteria that is in excellent agreement with experimental data from nanoscopic to macroscopic systems. These hybrid kirigami materials create new opportunities for multifunctional materials and structures, which we demonstrate with stretchable kirigami conductors with nearly constant electrical resistance up to $>$ 400 % strain and magnetoactive actuators with extremely rapid response ($>$ 10,000 % strain s^{-1}) and high, repeatable elongation ($>$ 300 %)

2.2 Introduction

Kirigami structures experience one of the two deformation modes between bending and rotation under loading, depending on the geometric design. However, the synergistic coupling of the two modes has not been explored, which could provide opportunities to further control stiffness and stretchability. In this chapter we present a new kirigami design that exhibits both ultra-soft mechanical response and large deformation. The in-plane deformation, or rotation, of the beams around the hinge and the out-of-plane deformation, or bending, of the beams allow for a significant decrease in stiffness by a factor of ~ 30 and an increase in ultimate sstrain by a factor of ~ 2. We apply the design principles to create resistance-invariant stretchable conductors and magnetoactive actuators with extremely rapid responses.

2.3 Background

The ability to tune the stiffness and deformation behavior of materials is critical to diverse applications from stretchable electronics and soft robotics to tissue engineering and biomedical devices. Someya et al. (2016); Tonazzini et al. (2016); Su et al. (2007); Morin et al. (2012); Dickey (2014); Chan et al. (2011); Mosadegh et al. (2014) Recently, techniques building upon principles in kirigami, the Japanese art of paper cutting, have demonstrated that the addition of cuts to materials enables elastic softening, large deformations, and the generation of 3D structures from 2D sheets across a range of length scales. Virk et al. (2013); Castle et al. (2016); Sussman et al. (2015); Neville et al. (2016); Castle et al. (2014); Hanakata et al. (2016); Liu et al. (2017) This enables the utilization of inextensible or functional components to create deformable devices such as reconfigurable electronics, optoelectronics, and sensors. Lamoureux et al. (2015); Someya et al. (2005); Sareh and Rossiter (2013); Iwata and Iwase (2017); Firouzeh and Paik (2015); Song et al. (2015); Lee et al. (2017); Yamamoto et al. (2016); Saha et al. (2017); Guo et al. (2016); Wang et al. (2017); Dias et al. (2017) As kirigami features generate geometric deformations that dominate the inherent material elasticity, properties and structures of kirigami metamaterials are controlled by the pattern and orientation of the cuts. This has been examined by recent efforts to concentrate

deformations on either the bending of beams defined by cuts or by the rotation of hinges that separate these features. Isobe and Okumura (2016); Shyu et al. (2015); Rafsanjani and Bertoldi (2017); Cho et al. (2014); Tang et al. (2016); Gatt et al. (2015); Tang et al. (2015) However, exploring the synergistic coupling of these deformation modes has been limited and further cut architecture modification has the potential to provide significant gains in stiffness tunability and deformability in kirigami metamaterials.

2.4 Approach

Here we show that the addition of minor cuts to kirigami structures provides a mechanism to control kirigami deformation modes for highly tunable mechanical response. We investigate this approach in polymeric films by adding minor cuts near the ends of major cuts to prescribe boundary conditions and create non-prismatic kirigami beams. This reduces stiffness by a factor of 30 and increases ultimate tensile strain by a factor of 2 relative to single incision patterns. Experimental results are supported by theoretical predictions in which the addition of minor cuts of various lengths and proximity to major cuts provides an analogous response to varying boundary conditions and beam geometry. We generalize these equations and provide design rules for kirigami films with tunable stiffness and extension responses and find excellent agreement between predictions and experimental measurements from nanoscopic to macroscopic kirigami materials. This approach and corresponding design criteria provide a simple and scalable method for the control of stiffness and deformation of materials without changing sample size, major pattern geometry, or material composition. We demonstrate the utility of this approach in stretchable electronics with highly stretchable conductors for deformable kirigami circuitry and in programmable matter with a rapid magnetoactive soft actuator. Both examples show that minor cuts enable a significant enhancement in deformability and stiffness control.

2.5 Experimental

Materials and mechanical measurements: Kirigami sheets are prepared by laser cutting (Epilog Laser Fusion M2, 75 watt) PET films (Grainger, $E = 2.62 \pm 0.1$ GPa). The elastic modulus of pristine PET films is calculated from the initial, linear regime ($\varepsilon \ll 1\%$) of a force-extension plot, captured with a 10kN load cell on an Instron 5944. The kirigami patterns on the PET film consist of slender beams (l_M = 20, 30 mm) with rectangular cross-section (w = 2, 3, 4 mm, t = 0.13 mm). N_B (= 2) is the number of beams in each row and N_{rows} (= 30) is the number of rows along the loading direction. The patterned region had lengths of $N_{rows}w \cong$ 60, 90, 120 mm and widths of $2l_M + 3d \cong$ 46, 66 mm. Pristine regions at both ends of kirigami patterns are clamped during testing. Three samples are tested under uniaxial tension for each design and geometry (Figure 2.4a) using an Instron 5944 mechanical testing machine with a 50 N load cell at a displacement rate of 1mm/s. Mechanical parameters are analyzed and calculated using MATLAB.

Stretchable electronics demonstration: PET kirigami films are spray coated with an eutectic indium-gallium (EGaIn) electrode and thin copper film leads are attached to the plain regions of the kirigami sheets for electrical measurements. Kirigami films are clamped into the grips of an Instron 5944 as in the mechanical measurements and resistance is measured with a four-point probe method by attaching leads to the copper tape at each end of the sample. Electrical data is collected with a Keithley 2460 (Keithley Instruments. Inc.) and is synchronized with the mechanical measurements with a digital trigger. Furthermore, the electronics shown in Figure 4c are fabricated by soldering LEDs onto copper film at each end of the sample.

Kirigami actuator: The kirigami actuator is composed of a single layer of patterned magneto-elastomer composite. It is a 820μm thick film of polydimethylsiloxane (PDMS) elastomer (Sylgard 184 with a 10:1 base-to-curing agent ratio; Dow Corning) with 70% w/w 1 μm Fe microparticles (US Research Nanomaterials Inc.). The sample is prepared by hand-mixing the PDMS and microparticles with a rod for 10 min followed by vacuum mixing in a planetary mixer (FlackTek Inc.; DAC 400.2 VAC) for complete dispersion. The Fe-PDMS mixture is cast onto a clean glass plate to form an even layer using a thin-film applicator (ZUA 2000; Zehntner Testing Instruments). This

is cured at 70 °C for 4 h. and then patterned with a CO_2 laser cutter to generate kirigami films. The magnetic field is generated by an electromagnet (Bunting Magnetics Co.) connected to a DC power supply providing a step function current of 4.0 A for 1 s and then off for 1 s. For high cycle testing, the magnet is powered off periodically to prevent overheating. The slow motion of the actuator was recorded at 240 fps with iPhone 6 and the recorded video was analyzed with a video analysis tool (Tracker; Open Source Physics).

2.6 Results and Discussion

2.6.1 Kirigami sheets consisting of prismatic beams

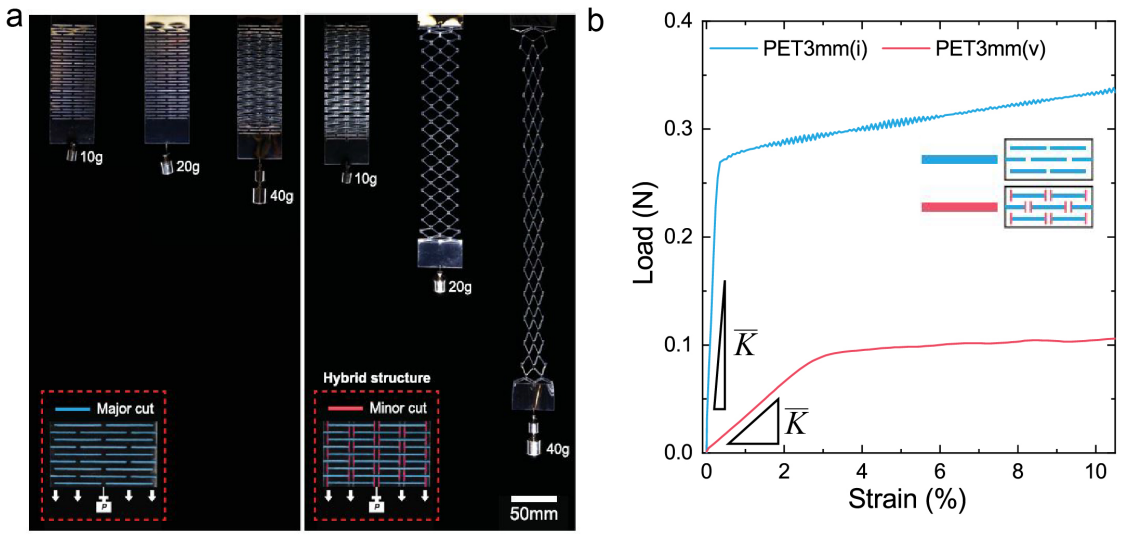

Figure 2.1 (a) Photographs of kirigami sheets with (left) only major cuts (Figure 2a (design i)) and (right) hybrid structures of major and minor cuts (Figure 2a (design v)). The same increasing weights (10 g, 20 g, and 40 g) are attached to each kirigami sheet to demonstrate mechanical response. Major cuts are highlighted in blue and the minor cuts are highlighted in red in the insets. (b) Load (P) versus strain (ε) for kirigami materials with design i of $w = 3$mm (blue curve) and with design v of $w = 3$mm and $l_m/2w = 0.75$ (red curve). Geometric parameters are described in Figure 2.4a. The slope indicates the effective in-plane stiffness.

Kirigami patterns are created in polyethylene terephthalate (PET) sheets ($E \approx 2.6$ GPa) with a CO_2 laser cutter. The patterned cuts consist of an array of transverse long major cuts, which define beams, and longitudinal short minor cuts, which prescribe beam shape and the rigidity of boundary conditions between beams. As seen in figure 2.1a, the addition of minor cuts significantly modifies the deformation behavior of kirigami film, resulting in a lower stiffness and higher elongation than a kirigami film consisting only of major cuts. Specifically, when hanging weights, a kirigami system consisting of only major cuts shows negligible strain ($\varepsilon \approx 0$ %) until the force reaches 0.4 N. In contrast, a modified system with major and minor cuts begins extending at a far lower force (≈ 0.1 N) and reaches strains over 270 % at a force of 0.4 N. The minor cuts also increase the ultimate extensibility of the films, as seen in figure 2.1b.

We consider the kirigami sheet as an array of slender beams with rectangular cross-section defined by the major cuts. Each beam is characterized by length l_M, width w, and thickness t with elastic modulus E. The spacing d between major cuts along the transverse direction and the thickness of samples are constant throughout the experiment ($d = 2$ mm, $t = 0.13$ mm). The length of minor cuts (l_m) is selected according to the dimensionless geometric parameter $l_m/2w = 0$, 0.25, 0.5, 0.75 and five different minor cut arrangements are investigated: i) no minor cuts, ii) minor cuts in between major cuts in alternating rows and iii) all rows, iv) minor cuts intersecting major cuts in alternating rows and v) all rows (figure 2.4a). Figure 2.1b shows a representative force-extension plot of a patterned sheet with and without minor cuts. Initially, the patterned sheet deforms with each beam bending in plane through the opening of cuts and rotation of plain regimes via hinges. As extension increases the in-plane beam bending becomes energetically more costly than out-of-plane bending, resulting in an elastic instability and a transition to out-of-plane beam bending (Figure 2.2). Isobe and Okumura (2016); Rafsanjani and Bertoldi (2017).

This continues until the deformation fully extends each beam, at which point the structure becomes loaded in tension, resulting in strain hardening and ultimately failure.

To analyze the mechanical behavior of these kirigami structures we consider an array of slender beams, where the stiffness of a single beam scales as $k \cong \frac{Ew^3t}{l_M^3}$, where E is the elastic modulus and

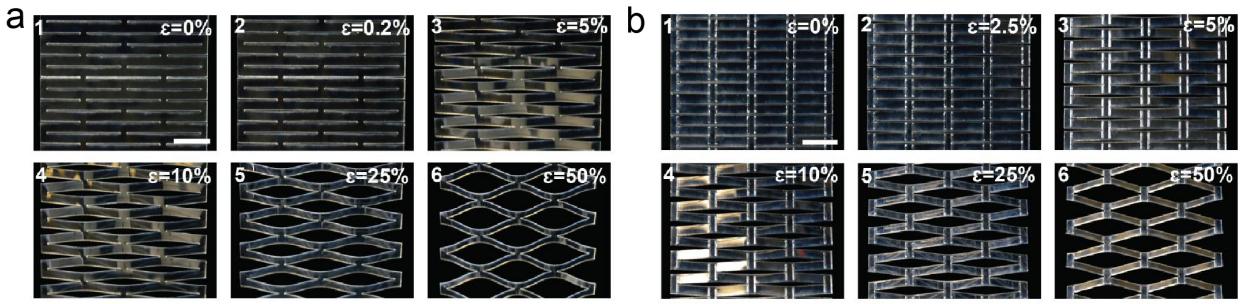

Figure 2.2 a) Image sequences of a krigiami structure without minor cuts (design i) and b) with minor cuts (design v) under uniaxial loading at the rate of 1mm/s. Scale bar : 10 mm. Geometric parameters in the structures are equivalent to those in Figure 1. The numbers in the top left corners of the image correspond to, 1 : Before tensile tests, 2: In-plane deformation, and 3-6 : Out-of-plane deformation.

l_M, w, and t are length, width, and thickness of the beam, respectively. Isobe and Okumura (2016) The effective in-plane stiffness $\overline{K}$ of the patterned sheet is calculated by considering of the number of beams and their arrangement (N_B/N_{rows}) such that:

$$\overline{K} = \alpha \frac{N_B}{N_{rows}} \frac{Ew^3t}{l_M^3} \tag{2.1}$$

where N_B is the number of beams in each row, N_{rows} is the number of rows along the loading direction, and α is a numerical coefficient which is dependent on boundary conditions and beam shape. As the major cuts define the primary beam dimensions l, w, t, minor cuts are introduced to explore the tunability of α. Figure 2.4b illustrates the stiffness dependence of a kirigami sheet on minor cuts as a function of the dimensionless minor cut parameter $l_m/(2w)$. Here, a kirigami sheet without minor cuts shows the highest stiffness while as minor cuts are introduced the stiffness decreases as $l_m/(2w)$ increases. Additionally, at each value of $l_m/(2w)$, stiffness decreases as the minor cuts intersect the major cuts and as the number of minor cuts increases. We consider that in the absence of minor cuts the ends of each beam are restrained from rotation and the in-plane bending occurs through the opening of major cuts and is analogous to a fixed-fixed end condition (FFE). As minor cuts are introduced near beam ends the FFE boundary conditions relax as the

hinge regions are softened and can no longer support bending moments resulting in a transition to pinned-pinned end conditions (PPE). This leads to deformations through the opening of major and minor cuts. To quantitatively describe this behavior the numerical coefficient α is calculated and is found to range between FFE ($\alpha = 16$) and PPE condition ($\alpha = 4$). These quantitative values are obtained as follows.

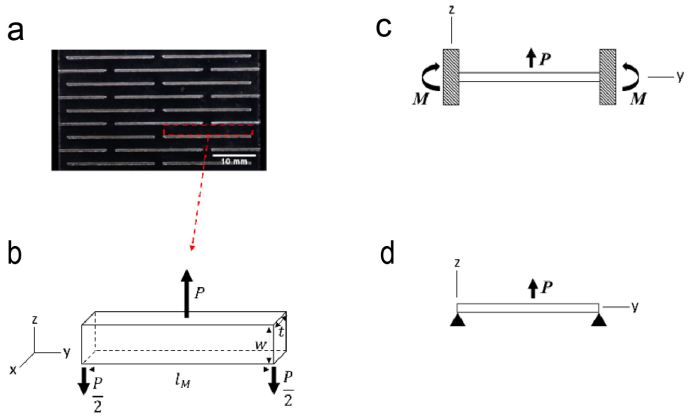

Figure 2.3 a) Kirigami film and b) schematic showing loading conditions. c) Fixed-fixed end conditions and d) pinned-pinned end conditions in a loaded beam.

As mentioned above, a sheet patterned wit hlinear cuts can be regarded as an array of beams (figure 2.3a and b). For the fixed-fixed end condition (figure 2.3c) at a small deflection, the differential equation of the deflection curve of the beam is

$$EI\frac{\partial^2\delta}{\partial x^2} = M(x) \tag{2.2}$$

, where the bending moment is

$$M(x) = \frac{P}{8}(4x - l_M), \quad (0 \leq x < \frac{l_M}{2}) \tag{2.3}$$

With boundary condition:

$$\frac{\partial\delta}{\partial x} = 0 \ \ at \ \ x = \frac{l_M}{2} \tag{2.4}$$

Where upon integration of equation (2.2) with boundary conditions in equation (2.4) we have the deflection at the midpoint, δ_C:

$$\delta_C = \frac{Pl_M^3}{192EI} \tag{2.5}$$

With $I = w^3t/12$, we obtain the stiffness (k):

$$k = 16\frac{Ew^3t}{l_M^3} \tag{2.6}$$

Where the numerical coefficient (α) is equal to $\alpha = 16$, which is dependent on boundary conditions and beam shape.

Next, for the pinned-pinned end condition (figure 2.3d) at a small deflection, the differential equation is

$$EI\frac{\partial^2\delta}{\partial x^2} = M(x) \tag{2.7}$$

, where the bending moment is

$$M(x) = \frac{P}{2}(x), \quad (0 \leq x < \frac{l_M}{2}) \tag{2.8}$$

With boundary condition:

$$\frac{\partial\delta}{\partial x} = 0 \;\; at \;\; x = \frac{l_M}{2} \tag{2.9}$$

Where upon integration of equation (2.7) with boundary conditions in equation (2.9) we have the deflection at the midpoint, δ_C:

$$\delta_C = \frac{Pl_M^3}{48EI} \tag{2.10}$$

With $I = w^3t/12$, we obtain the stiffness (k):

$$k = 4\frac{Ew^3t}{l_M^3} \tag{2.11}$$

Where the numerical coefficient (α) is equal to $\alpha = 4$, which is dependent on boundary conditions and beam shape.

When these bounds are plotted in Figure 2.4b. it is seen that the data falls within the bounds of these conditions for design *i-iv*, supporting the analogy of minor cuts to beam boundary conditions.

2.6.2 Kirigami sheets consisting of non-prismatic beams

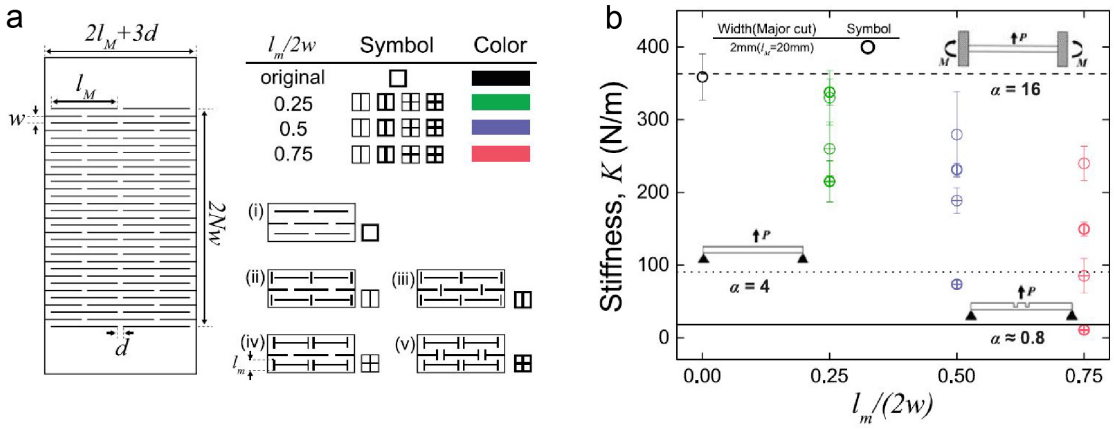

Figure 2.4 (a) A schematic of a kirigami structure with geometric parameters and different designs. Data point symbol represents each beam size, which is defined by major cuts, data point interior represents different minor cut designs, and data point color represents the ratio of minor cut length over width of beam. (b) Effective in-plane stiffness $\overline{K}$ versus $l_m/(2w)$ for varying pattern designs, with l_M = 20 mm, $w = d$ = 2 mm, and l_m= 0 - 3 mm. Dashed/dotted/solid lines represent Equation (2.1) with FFE ($\alpha = 16$), PPE ($\alpha = 4$), and non-prismatic beam/pinned end condition ($\alpha \approx 0.8$), respectively.

We further explore beam geometry by applying a kirigami design to create non-prismatic beams (Figure 2.4a(v)). In most cases, non-prismatic beams with varying moments of inertia along the length are employed for enhancing mechanical strength and stiffness. Gere and Timoshenko (1997) In contrast, we utilize this approach in the kirigami system to further reduce stiffness and obtain an *ultra-soft kirigami* structure. This is achieved by introducing minor cuts onto the beam midspan without changing major cut length. The design decreases the area moment of inertia in

regions where the bending moment is largest, resulting in an enhanced softening effect on the PPE condition. The derivation is as follows:

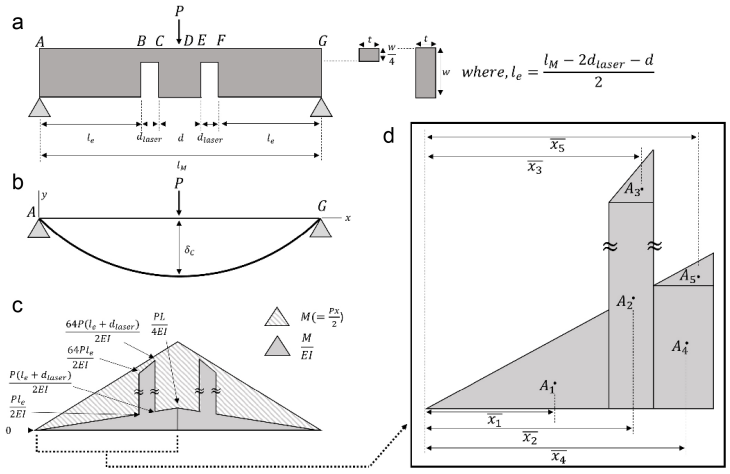

Figure 2.5 a) Schematic of non-prismatic beam with defined geometry and b) beam under load. c) *M/EI* diagram and d) detailed view of sections.

For a non-prismatic beam, where the flexural rigidity EI is not constant along the length, the stiffness is calculated using the moment-area method. Here we adopted a specific system with the following dimensions: $l_M = 20\text{mm}$, $l_e = 8.85\text{mm}$, $d_{laser} = 0.3\text{mm}$, $d = 0.85\text{mm}$, $l_{AB,CD} = 64 l_{BC}$. The area of the *M/EI* diagram, A_i, for the different segments of the beam are:

$$\begin{aligned} A_1 &= \frac{1}{2}(0.4425 l_M)(\frac{P(0.4425 l_M)}{2EI}) \quad A_2 = \frac{1}{2}(0.015 l_M)(\frac{64P(0.4425 l_M)}{2EI}) \\ A_3 &= \frac{1}{2}(0.015 l_M)(\frac{64P(0.015 l_M)}{2EI}) \quad A_4 = (0.0425 l_M)(\frac{64P(0.4575 l_M)}{2EI}) \\ A_5 &= \frac{1}{2}(0.0425 l_M)(\frac{P(0.0425 l_M)}{2EI}) \end{aligned} \tag{2.12}$$

The displacement is then calculated as:

$$\delta_C = A_1 \overline{x}_1 + A_2 \overline{x}_2 + A_3 \overline{x}_3 + A_4 \overline{x}_4 + A_5 \overline{x}_5 \tag{2.13}$$

where $\overline{x}_1 \sim \overline{x}_5$ are the distances between point A and the centroids of individual areas. These distances are:

$$\overline{x}_1 = \frac{2}{3}(0.4425 l_M);\ \ \overline{x}_2 = 0.4425 l_M + \frac{1}{2}(0.015 l_M);$$
$$\overline{x}_3 = 0.4425 l_M + \frac{2}{3}(0.015 l_M);\ \ \overline{x}_4 = 0.4575 l_M + \frac{1}{2}(0.0425 l_M); \tag{2.14}$$
$$\overline{x}_5 = 0.4575 l_M + \frac{2}{3}(0.0425 l_M);$$

The deflection at the midpoint, δ_C is then:

$$\delta_C = 0.116523 \frac{P l_M^3}{EI} \tag{2.15}$$

With $I = w^3 t/12$, we obtain the stiffness (k):

$$k \cong 0.7 \frac{E w^3 t}{l_M^3} \tag{2.16}$$

Where the numerical coefficient (α) is equal to $\alpha \approx 0.7$. For the case of a $l_M = 30$ mm beam, $\alpha \approx 0.9$. In the manuscript, both $l_M = 20$ mm and $l_M = 30$ mm beams are displayed on the same plot, for clarity of presentation we choose α is ≈ 0.8 when displaying theoretical predictions. The numerical coefficient of the non-prismatic beam (α is ≈ 0.8) is lower than the PPE condition ($\alpha = 4$), and is consistent with the trend in the data in Figure 2.4b.

Upon rearrangement of equation (2.1) the relation between effective stiffness and geometric parameters is $\overline{K}/Et = \alpha \frac{N_B}{N_{rows}} (w/l_M)^3$. Figure 2.6a presents a log-log plot of our experimental data with 52 combinations of major (two different lengths l_M =20 mm, 30 mm and three different widths $w = 2$ mm, 3 mm, and 4 mm) and minor cuts and shows that the data for prismatic beams collapses into the range bounded by FFE and PPE conditions. Some deviation from this prediction is observed as $l_M \leq 5w$, which was also observed by Isobe *et al.*, Isobe and Okumura (2016) as the beam begins to violate the slender beam assumption. The stiffness is greatly reduced by constructing kirigami structures with non-prismatic beams. When design (v) with 0.75 $l_m/(2w)$ is adopted, which shows the smallest moment of inertia in the midspan of our designs, the stiffness decreases by a factor of ≈22-30 compared to systems consisting only of major cuts. The stiffness data for this non-prismatic beam continues to follow the scaling prediction with $\alpha \approx 0.8$. Additionally, the

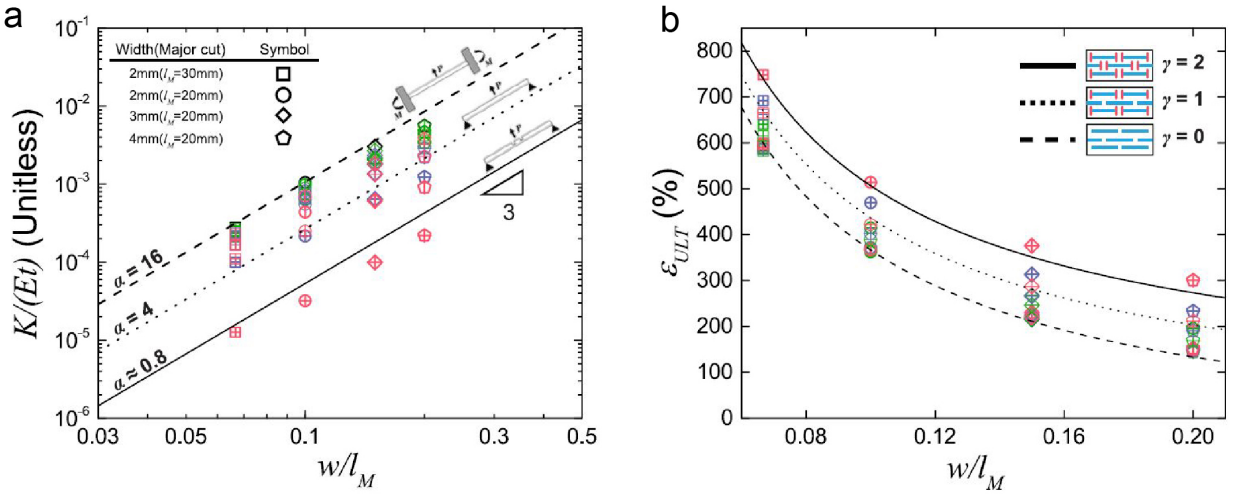

Figure 2.6 $\overline{K}/Et$ versus w/l_M with varying major and minor cut conditions, dashed/dotted/solid lines represent the same α values as in component (b) in figure 2.4b. (d) Ultimate strain (ϵ_{ULT}) versus w/l_M, where lines represent Equation 3 with various γ values as specified in the legend.

ultra-soft kirigami structure shows significantly reduced stiffness compared to a design with just major cuts throughout the entire strain range (Figure 2.7).

These dramatic changes in stiffness through the α parameter by controlling boundary conditions and moment of inertia along the beam greatly increases design flexibility of kirigami materials, especially in systems with size limitations or fabrication constraints.

2.6.3 Ultimate strain for kirigami sheets

In addition to the control of initial stiffness, kirigami structures can also tune the ultimate strain (ε_{ULT}) of materials. Figure 2.6b illustrates the ultimate strain of each system with different geometries and arrays of minor cuts as a function of a dimensionless major cut parameter w/l_M. As the width-length ratio w/l_M decreases, the ultimate strain increases as beams become relatively longer with regards to their cross-section (wt), resulting in larger axial displacements. In addition, the ultimate strain is affected by the array of minor cuts. The lowest ultimate strain is

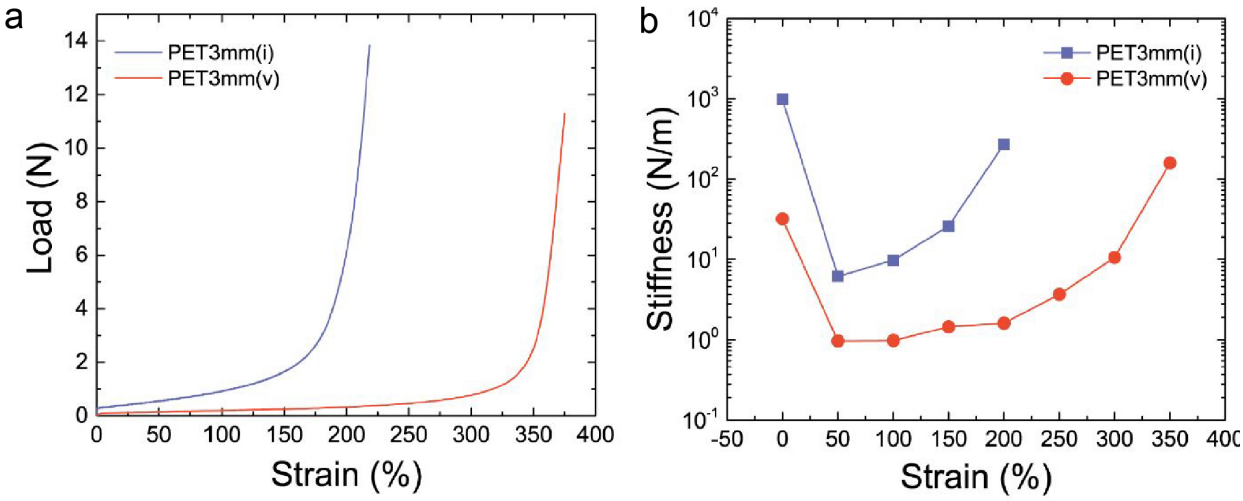

Figure 2.7 a) Load (P) versus strain (ϵ)r kirigami materials with design i of $w = 3$mm (blue curve) and with design v of $w = 3$mm and $l_m/2w = 0.75$ (red curve). See Figure 2.1b to see a close-up view of the initial regime of both patterned structures of the P - ϵ plot. The slope indicates the effective in-plane stiffness. b) Log-linear plot of Stiffness versus strain for equivalent designs and geometric parameters. Effective in-plane stiffness ($\epsilon = 0\%$) and effective out-of-plane stiffness $\epsilon > 0\%$ are calculated by linearly fitting experimental data points with a 5 % strain window every 50%.

achieved utilizing only major cuts, whereas the highest is achieved for hybrid cuts with design v and $l_m/(2w) = 0.75$. To predict ultimate strain where kirigami sheets break, we derive a model based on beam geometry at ultimate strain. Here, we assume $w, d \ll l_M$ and expand previous models Shyu et al. (2015) to include minor cuts and the reduction of ε_{ULT} by edge effects such that:

$$\varepsilon_{ULT} \cong \frac{(N_{rows} - 2)\,(l_M + \gamma l_m)}{2N_{rows}w} - 1 \tag{2.17}$$

where γ is a numerical coefficient to account for the contribution of minor cuts to ε_{ULT}; $\gamma = 0$ in the absence of minor cuts (design i), $\gamma = 1$ or 2 in the presence of minor cuts in alternating rows (design iv) or every row (design v), respectively. The full derivation is as follows:

To predict ultimate strain where kirigami sheets break, we derive an empirical formula based on work by Isobe et al and Shyu et al. Isobe and Okumura (2016); Shyu et al. (2015) Their approach

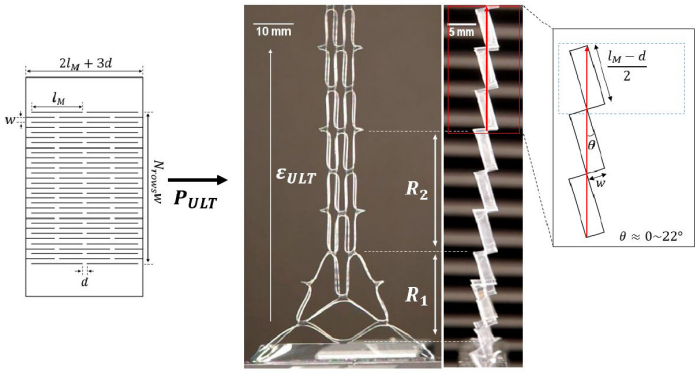

Figure 2.8 Stretching of kirigami film without minor cuts to examine ultimate stretching behavior.

assumes that all the beams deform in the same manner. However, when the number of rows N_{rows} along the axial direction is finite, this can overestimate ϵ_{ULT} due to edge effects. At the edge of the sample there is a region of reduced displacement, R_1, compared to regions of uniform displacement, R_2, away from the edges (Figure 2.9). Experimentally, we find the rduction of displacement in the initial and final regimes to be $R_1/R_2 \approx 0.7$, as summarized in Table 2.1. In addition, each beam cannot perfectly align along the loading direction due to the connectivity between beams. This results in a finite angle between the beam and the loading direction, as seen in Figure 2.9, which upon performing image analysis on samples stretched to ϵ_{ULT} varies between $\theta \approx 0° \sim 22°$ in our system for $l_M \geq 5w$ (see Table 2.1 for details).

Table 2.1 Edge effects and beam angle in direction of loading at ϵ_{ULT}

w/l_M	**2/30**	**2/20**	**3/20**	**4/20**
	29.35/43.74	22.12/30.30	22.46/30.58	23.40/32.78
R_1/R_2	30.14/44.98	21.71/30.40	22.22/31.04	23.77/32.10
	30.68/45.01	21.82/30.38	21.78/30.55	22.90/32.08
θ	8°	10°	18°	22°
Average	0.674	0.721	0.721	0.723

When taking into account edge effects and the finite angle upon maximum extension we find that the ultimate length of the sample, L_{ULT}, can be calculated as:

$$L_{ULT} = N_{rows}\sqrt{w^2 + \left(\frac{l_M - d}{2}\right)^2} - 2 \times N_{rows,edg} \times \left(1 - \left(\frac{R_1}{R_2}\right)\right)\sqrt{w^2 + \left(\frac{l_M - d}{2}\right)^2} \tag{2.18}$$

Or

$$L_{ULT} = N_{rows}\frac{l_M - d}{2cos\theta} - 2 \times N_{rows,edg} \times \left(1 - \left(\frac{R_1}{R_2}\right)\right)\frac{l_M - d}{2cos\theta} \tag{2.19}$$

Where $N_{rows,edg}$ is the number of rows under the influence of edge effects. According to images of samples throughout experiments, the first 3 and last 3 rows show significant edge effect ($N_{rows,edg}$ = 3). The numerical value 2 before $N_{rows,edg}$ takes into account both end regimes along the loading direction. When 1-(R_1/R_2) ≈ 0.3, Equation (2.18) and (2.19) can be simplified with the assumption that $N_{rows,edg}$ × (1-(R_1/R_2)) ≈ 1:

$$L_{ULT} = N_{rows}\frac{l_M - d}{2cos\theta} \tag{2.20}$$

With $L_0 = N_{rows}w$, the ultimate strain can be defined as:

$$\epsilon_{ULT} = \frac{\Delta L}{L_0} = \frac{L_{ULT} - L_0}{L_0} = \frac{(N_{rows} - 2)\frac{l_M - d}{2cos\theta}}{N_{rows}w} - 1 \tag{2.21}$$

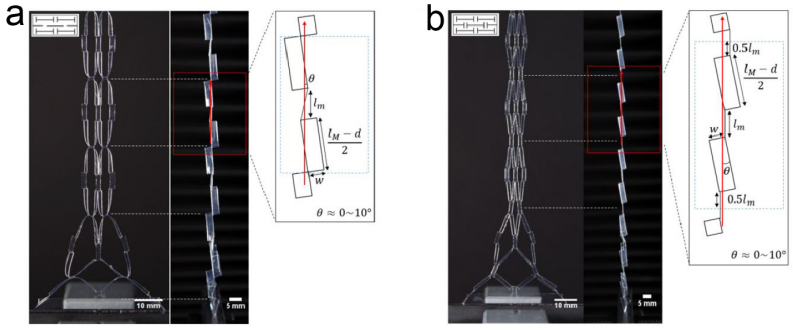

Figure 2.9 Stretching of kirigami film with minor cuts in a) alternating rows and b) every row to examine ultimate stretching behavior.

In our system, we introduce minor cuts into a kirigami structure containing major cuts. This modification leads to a change in ultimate strain due to the opening up of minor cuts by a factor of

γl_m, where $\gamma = 0$, 1, 2 for no minor cuts, minor cuts on alternating rows, and minor cuts in every row respectively and l_m is the length of the minor cut. Thus, the ultimate length of the sample, L_{ULT}, can be calculated as:

$$L_{ULT} = (N_{rows} - 2)\left(\frac{l_M - d + \gamma l_M}{2cos\theta}\right) \tag{2.22}$$

With $L_0 = N_{rows}w$, the ultimate strain is then:

$$\epsilon_{ULT} = \frac{\Delta L}{L_0} = \frac{(N_{rows} - 2)\left(\frac{l_M - d + \gamma l_M}{2cos\theta}\right)}{N_{rows}w} - 1 \tag{2.23}$$

If the kirigami structure is composed of slender beams with relatively short spacing such that $l_M \gg w, d$ so $cos\theta \to 1$, and the number of rows is large so that $N_{rows} - 2 \approx N_{rows}$, equation (2.23) can be simplified to:

$$\epsilon_{ULT} = \frac{1_M + \gamma l_m}{2w} - 1 \tag{2.24}$$

We have adopted this simplified equation when calculating $\frac{\gamma_{ULT}}{K}$.This can also be examined as the ultimate stretch ratio, $\gamma_{ULT} = L_{ULT}/L_0$, and can be calculated as $\gamma_{ULT} \approx \frac{1_M + \gamma l_m}{2w}$.

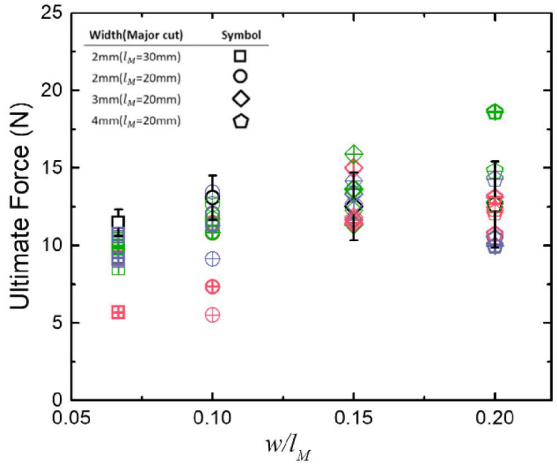

Figure 2.10 Ultimate force of kirigami materials. See Figure 2.4a for key to symbol color and fill pattern

Upon plotting ε_{ULT} as a function of w/l_M, we find excellent agreement between the experimental data and Equation (2.17). When minor cuts are included it enables further rotation of hinge regions by opening of minor cuts, as indicated by the increase in ε_{ULT} for a fixed value of beam aspect ratio (w/l_M). Further, we find that the force at break of low to moderate aspect ratio beams ($w/l_M \geq 0.15$) is not significantly influenced by minor cuts, with a slight decrease for very slender beams ($w/l_M \leq 0.1$) (Figure 2.10). This can be attributed to the thin hinge regions and can be further improved by reducing stress concentrations through rounded corners as previously demonstrated. Tang et al. (2015) Thus, minor cuts provide an additional means to increase and tune the strain at break for kirigami materials.

2.6.4 General relationship for the design of kirigami structures

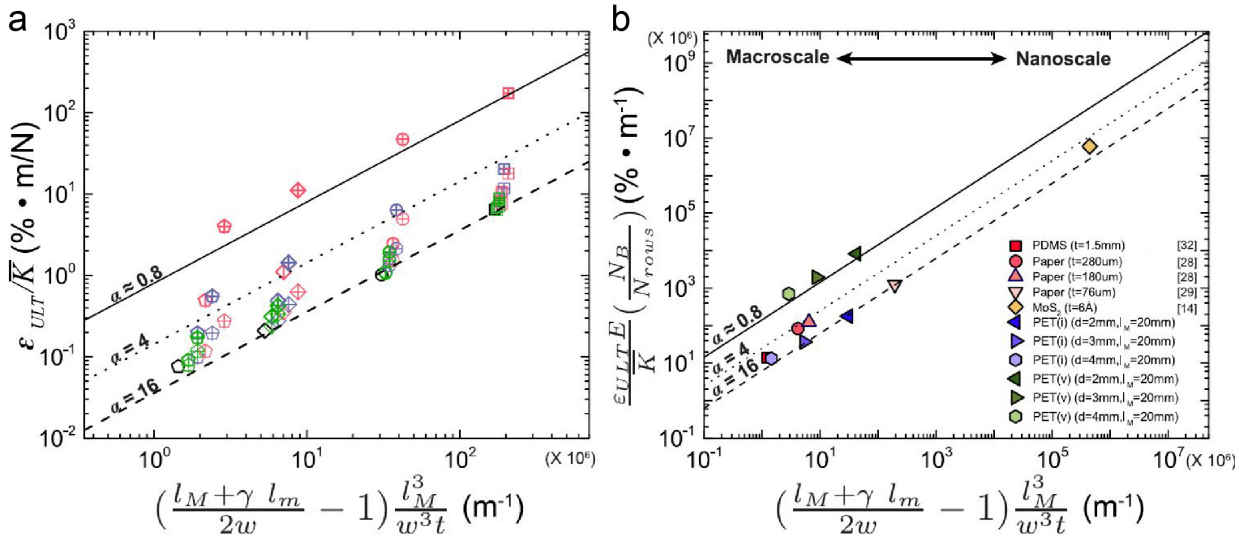

Figure 2.11 (a) Mechanical property $\epsilon_{ULT}/\overline{K}$ versus a combined geometric parameter for all the data in this work, where lines represent Equation (2.25). (b) Scaling plot showing agreement between Equation 3 and experimental/simulation data from kirigami materials in the literature and from the current work, across a wide range of length scales and material classes.

To provide a general relationship for the design of kirigami structures consisting of arrays of beams for high extensibility and low stiffness, we combine Equations (2.1) and (2.17) such that:

$$\frac{\varepsilon_{ULT}}{\overline{K}} = \frac{1}{E\alpha}\left(\frac{N_{rows}}{N_B}\right)\left(\frac{l_M + \gamma\ l_m}{2w} - 1\right)\frac{l_M^3}{w^3 t} \tag{2.25}$$

Equation (2.25) shows that the mechanical response of kirigami structures is controlled by the geometry (l_M, w, t) and arrangement (N_{rows}, N_B) of beams, which are defined by major cuts, the arrangement/length of minor cuts (α, l_m, γ), and the elastic properties (E) of the film. The ultimate strain with regards to effective stiffness $\varepsilon_{ULT}/\overline{K}$ is proportional to the number of beams along the loading axis N_{rows} and the length of beams (l_M, l_m) and is inversely proportional to Young's modulus of intrinsic materials E, boundary conditions (determined by the arrangement of minor cuts) α, the number of beams per row N_B, and the width and thickness of beams (w, t). Note from the result that the fourth order of the length and width of the beam play a critical role in designing ultra-soft and highly stretchable kirigami structures (i.e., large $\varepsilon_{ULT}/\overline{K}$).

Upon plotting $\varepsilon_{ULT}/\overline{K}$ as a function of major and minor cut geometry in Figure 2.11a, we find good agreement between the predictions and experimental data, where α provides a mechanism to tune the ratio of $\varepsilon_{ULT}/\overline{K}$ for a fixed beam geometry. As this equation is composed of geometric and material properties we expect the predictions to function over a wide range of scales from nanoscopic to macroscopic size scales. By rearranging Equation (2.25) to normalize for the number of beams in the system, we plot diverse experimental and simulation data from kirigami studies in literature along with our data in Figure 2.11b. We observe that all the data with only major patterns collapse into a region bounded by $\alpha = 4$ and $\alpha = 16$ while the addition of minor cuts is captured with $\alpha = 0.8$. This analysis describes the behavior of kirigami materials from sub-nanometer to millimeter film thickness with diverse material classes. Although nano-scale effects may influence the scaling at nanometer dimensions, the presented results and analysis provide evidence for the scalability of kirigami materials across tremendous length scales.

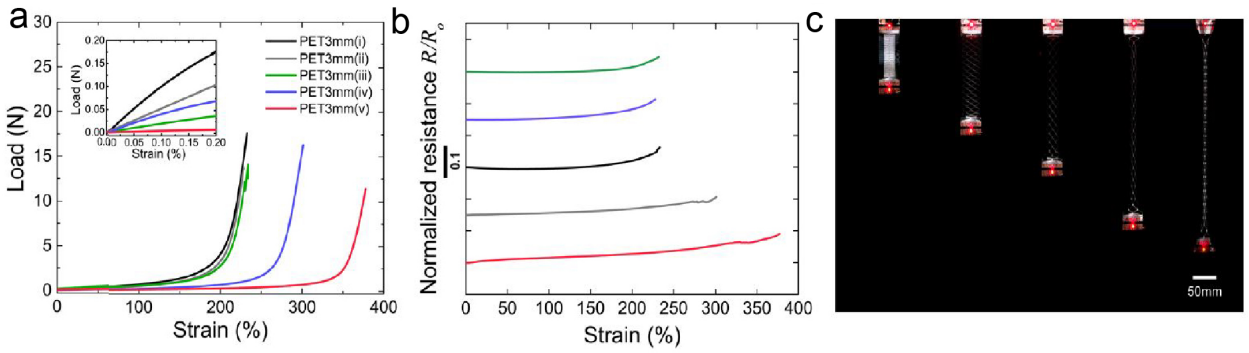

Figure 2.12 (a) Load versus strain plot for kirigami stretchable electrodes with various hybrid designs. The inset shows the tunable stiffness in the initial regime (l_M = 20 mm, l_m = 4.5 mm, w = 3 mm). (b) Normalized resistance versus strain plot showing that the electrical resistance for each design remains largely constant through failure. (c) Demonstration of hybrid kirigami structures as stretchable interconnects under axial deformation up to 380 % strain.

2.6.5 Applications : Stretchable conductors and magnetoactive actuators

As our kirigami films are mechanically compliant and highly deformable, they enable opportunities to create multifunctional materials for soft and stretchable electronics and components for soft robotics. To investigate their use as stretchable conductors we add a conductive liquid metal electrode on top of kirigami films with a range of minor cut conditions and measure electrical resistance as a function of strain. We find that the electrical resistance of all the samples remains largely unchanged upon deformation, but the addition of minor cuts allows the stiffness and ultimate strains to be tuned (Figure 2.12). In the case of an ultra-soft kirigami film, the electrical resistance increases by less than 10 % up to a strain of 380 % (Figure 2.12b). The viability of kirigami as stretchable interconnects is demonstrated with a LED circuit (Figure 2.12c), where the addition of minor cuts allows for strains up to ∼400 %, compared to ∼230 % with only major cuts. The LED is illuminated up to the breaking strain, showing the potential to create kirigami interconnects with easily tunable stiffness and deformation properties for stretchable electronic applications.

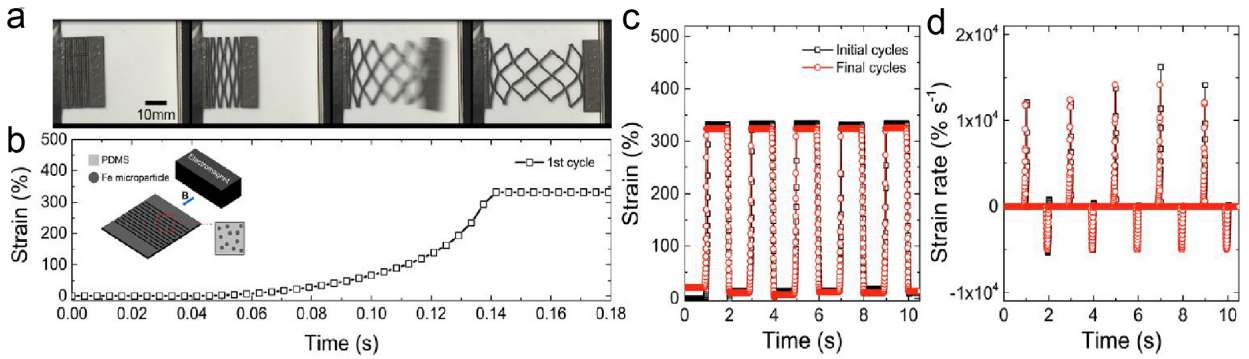

Figure 2.13 (a) High speed photographs of a magnetoactive hybrid kirigami structure made of Fe-PDMS with design v (l_M = 15 mm, l_M = 1.3 mm, w = 0.9 mm, and t = 0.82 mm) in response to a magnetic field. (b) Strain versus time plot of the patterned sample during the first cycle and (c) during the initial cycling and after $\sim$ 1000 cycles (final cycles) maintaining a large deformation ($\sim$ 330%). (d) Strain rate versus time plot of the sample during the initial cycles and final cycles, showing rapid motion in response to a magnetic field.

Furthermore, we show how our kirigami materials can be used as actuators or reconfigurable matter by creating magnetoactive soft actuators. Samples are fabricated by embedding Fe microparticles into a matrix of polydimethylsiloxane (PDMS) and then laser machining kirigami patterns into the cured composite. When a kirigami actuator with hybrid cut patterns (design v) is activated by an electromagnet, the sheet rapidly elongates to 330 % strain in $\sim$ 0.1 s with a maximum strain rate during the cycle greater than 10,000 % s^{-1} (Figure 2.13a and b). By alternating the magnetic field on/off at 1 s intervals, the hybrid kirigami actuator is activated and released over 1,000 cycles without degradation in speed or stroke (Figure 2.13c and d). This approach to adaptive soft actuators enables an unique and exceptional combination of high-speed actuation, large deformation, and stable reversibility, outperforming nearly all other soft matter actuators and morphing technologies.Nguyen et al. (2012); Zhao et al. (2014) By further tuning hybrid cut structures and material choice the actuators can respond and adapt to different stimuli across a range of length scales, providing a rich design space for multifunctional materials and structures.

2.7 Conclusion

In summary, the synergistic mechanical coupling of hybrid major and minor cuts in kirigami materials enables highly tunable mechanical metamaterials. These hybrid structures can introduce effective boundary conditions and non-prismatic structures which can be quantitatively captured by the numerical coefficient α, which in the current work was varied in the range of $0.8 \leq \alpha \leq 16$. However, α can be further controlled and decreased to create softer kirigami structures by increasing the length and number of minor cuts to further increase the proportion of regions where the moment of inertia is small. This approach can be used to increase the mechanical response of materials to external stimuli such as mechanical force, magnetic or electrical fields, or chemical triggers. We show how these hybrid structures can be used to create ultra-soft and highly deformable multifunctional materials such as stretchable conductors with nearly invariable resistance to extreme strain and actuators with rapid response and high elongation. The mechanical response of hybrid kirigami materials is well captured by our analytical expressions and leads to compact design criteria which can be used to efficiently create kirigami-based materials for diverse applications across a wide range of length scales.

2.8 References

Castle, T., Cho, Y., Gong, X., Jung, E., Sussman, D. M., Yang, S., and Kamien, R. D. (2014). Making the cut: Lattice kirigami rules. *Physical Review Letters*, 113(24):245502.

Castle, T., Sussman, D. M., Tanis, M., and Kamien, R. D. (2016). Additive lattice kirigami. *Science Advances*, 2(9):e1601258–e1601258.

Chan, E. P., Walish, J. J., Thomas, E. L., and Stafford, C. M. (2011). Block copolymer photonic gel for mechanochromic sensing.

Cho, Y., Shin, J.-H., Costa, A., Kim, T. A., Kunin, V., Li, J., Lee, S. Y., Yang, S., Han, H. N., Choi, I.-S., and Srolovitz, D. J. (2014). Engineering the shape and structure of materials by fractal cut. *Proceedings of the National Academy of Sciences of the United States of America*, 111(49):17390–5.

Dias, M. A., McCarron, M. P., Rayneau-Kirkhope, D., Hanakata, P. Z., Campbell, D. K., Park, H. S., and Holmes, D. P. (2017). Kirigami Actuators. *Soft Matter*.

Dickey, M. D. (2014). Emerging applications of liquid metals featuring surface oxides. *ACS Applied Materials and Interfaces*, 6(21):18369–18379.

Firouzeh, A. and Paik, J. (2015). The Design and Modeling of a Novel Resistive Stretch Sensor with Tunable Sensitivity. *IEEE Sensors Journal*, 15(11):6390–6398.

Gatt, R., Mizzi, L., Azzopardi, J. I., Azzopardi, K. M., Attard, D., Casha, A., Briffa, J., and Grima, J. N. (2015). Hierarchical Auxetic Mechanical Metamaterials. *Scientific Reports*, 5:8395.

Gere, J. M. and Timoshenko, S. P. (1997). *Mechanics of Materials*. PWS Publishing Company, 4th edition.

Guo, H., Yeh, M. H., Lai, Y. C., Zi, Y., Wu, C., Wen, Z., Hu, C., and Wang, Z. L. (2016). All-in-One Shape-Adaptive Self-Charging Power Package for Wearable Electronics. *ACS Nano*, 10(11):10580–10588.

Hanakata, P. Z., Qi, Z., Campbell, D. K., and Park, H. S. (2016). Highly stretchable MoS2 kirigami. *Nanoscale*, 8(1):458–463.

Isobe, M. and Okumura, K. (2016). Initial rigid response and softening transition of highly stretchable kirigami sheet materials. *Scientific Reports*, 6(April):24758.

Iwata, Y. and Iwase, E. (2017). Stress-Free Stretchable Electronic Device. *Micro Electro Mechanical Systems (MEMS)*, 2017 IEEE:231–234.

Lamoureux, A., Lee, K., Shlian, M., Forrest, S. R., and Shtein, M. (2015). Dynamic kirigami structures for integrated solar tracking. *Nature Communications*, 6:8092.

Lee, Y. K., Jang, K.-I., Ma, Y., Koh, A., Chen, H., Jung, H. N., Kim, Y., Kwak, J. W., Wang, L., Xue, Y., Yang, Y., Tian, W., Jiang, Y., Zhang, Y., Feng, X., Huang, Y., and Rogers, J. A. (2017). Chemical Sensing Systems that Utilize Soft Electronics on Thin Elastomeric Substrates with Open Cellular Designs. *Advanced Functional Materials*, 201605476:1605476.

Liu, Y., Shaw, B., Dickey, M. D., and Genzer, J. (2017). Sequential self-folding of polymer sheets. *Science Advances*, 3:1–7.

Morin, S. A., Shepherd, R. F., Kwok, S. W., Stokes, A. A., Nemiroski, A., and Whitesides, G. M. (2012). Camouflage and display for soft machines. *Science*, 337(6096):828–32.

Mosadegh, B., Polygerinos, P., Keplinger, C., Wennstedt, S., Shepherd, R. F., Gupta, U., Shim, J., Bertoldi, K., Walsh, C. J., and Whitesides, G. M. (2014). Pneumatic networks for soft robotics that actuate rapidly. *Advanced Functional Materials*, 24(15):2163–2170.

Neville, R. M., Scarpa, F., and Pirrera, A. (2016). Shape morphing Kirigami mechanical metamaterials. *Scientific Reports*, 6(1):31067.

Nguyen, V. Q., Ahmed, A. S., and Ramanujan, R. V. (2012). Morphing soft magnetic composites. *Advanced Materials*, 24(30):4041–4054.

Rafsanjani, A. and Bertoldi, K. (2017). Buckling-Induced Kirigami. *Physical Review Letters*, 118(8):84301.

Saha, B., Baek, S., and Lee, J. (2017). Highly Sensitive Bendable and Foldable Paper Sensors Based on Reduced Graphene Oxide. *ACS Applied Materials & Interfaces*, 9(5):4658–4666.

Sareh, S. and Rossiter, J. (2013). Kirigami artificial muscles with complex biologically inspired morphologies. *Smart Materials and Structures*, 22(1):014004.

Shyu, T. C., Damasceno, P. F., Dodd, P. M., Lamoureux, A., Xu, L., Shlian, M., Shtein, M., Glotzer, S. C., and Kotov, N. A. (2015). A kirigami approach to engineering elasticity in nanocomposites through patterned defects. *Nature Materials*, 14(8):785–789.

Someya, T., Bao, Z., and Malliaras, G. G. (2016). The rise of plastic bioelectronics. *Nature*, 540(7633):379–385.

Someya, T., Kato, Y., Sekitani, T., Iba, S., Noguchi, Y., Murase, Y., Kawaguchi, H., and Sakurai, T. (2005). Conformable, flexible, large-area networks of pressure and thermal sensors with organic transistor active matrixes. *Proceedings of the National Academy of Sciences of the United States of America*, 102(35):12321–12325.

Song, Z., Wang, X., Lv, C., An, Y., Liang, M., Ma, T., He, D., Zheng, Y.-J., Huang, S.-Q., Yu, H., and Jiang, H. (2015). Kirigami-based stretchable lithium-ion batteries. *Scientific Reports*, 5:10988.

Su, Y.-F., Kim, H., Kovenklioglu, S., and Lee, W. (2007). Continuous nanoparticle production by microfluidic-based emulsion, mixing and crystallization. *Journal of Solid State Chemistry*, 180(9):2625–2629.

Sussman, D. M., Cho, Y., Castle, T., Gong, X., Jung, E., Yang, S., and Kamien, R. D. (2015). Algorithmic lattice kirigami: A route to pluripotent materials. *Proceedings of the National Academy of Sciences*, 112(24):7449–7453.

Tang, J., Wang, J., Liu, J., and Zhou, Y. (2016). Jumping liquid metal droplet in electrolyte triggered by solid metal particles. *Applied Physics Letters*, 108(22):223901.

Tang, Y., Lin, G., Han, L., Qiu, S., Yang, S., and Yin, J. (2015). Design of Hierarchically Cut Hinges for Highly Stretchable and Reconfigurable Metamaterials with Enhanced Strength. *Advanced Materials*, 27(44):7181–7190.

Tonazzini, A., Mintchev, S., Schubert, B., Mazzolai, B., Shintake, J., and Floreano, D. (2016). Variable Stiffness Fiber with Self-Healing Capability. *Advanced Materials*, 28(46):10142–10148.

Virk, K., Monti, a., Trehard, T., Marsh, M., Hazra, K., Boba, K., Remillat, C. D. L., Scarpa, F., and Farrow, I. R. (2013). SILICOMB PEEK Kirigami cellular structures: mechanical response and energy dissipation through zero and negative stiffness. *Smart Materials and Structures*, 22(8):084014.

Wang, W., Li, C., Rodrigue, H., Yuan, F., Han, M. W., Cho, M., and Ahn, S. H. (2017). Kirigami/Origami-Based Soft Deployable Reflector for Optical Beam Steering. *Advanced Functional Materials*, 27(7):1604214.

Yamamoto, Y., Harada, S., Yamamoto, D., Honda, W., Arie, T., Akita, S., and Takei, K. (2016). Printed multifunctional flexible device with an integrated motion sensor for health care monitoring. *Science Advances*, 2(11):e1601473–e1601473.

Zhao, Q., Dunlop, J. W. C., Qiu, X., Huang, F., Zhang, Z., Heyda, J., Dzubiella, J., Antonietti, M., and Yuan, J. (2014). An instant multi-responsive porous polymer actuator driven by solvent molecule sorption. *Nature communications*, 5:4293.

CHAPTER 3. KIRIGAMI-ENABLED, PASSIVE RESONANT SENSORS FOR WIRELESS DEFORMATION MONITORING

Sadaf Charkhabi,[1] Yee Jher Chan,[1] Doh-Gyu Hwang,[2] Sean T. Frey,[2] Michael D. Bartlett,[2] and Nigel F. Reuel[1]

[1] Department of Chemical and Biological Engineering, Iowa State University, Ames, IA 50011, USA

[2] Department of Materials Science and Engineering, Soft Materials and Structures Lab, Iowa State University, Ames, IA 50011, USA

Modified from a manuscript published in *Advanced Materials Technologies*

3.1 Abstract

A passive resonant sensor with kirigami patterning is presented to wirelessly report material deformation in closed systems. The sensors are fabricated from copper-coated polyimide by etching a conductive Archimedean spiral and then laser cutting kirigami patterns. The sensor response is defined as the resonant frequency in the transmission scattering parameter signal (S_{21}), which is captured via a benchtop vector network analyzer. The sensors are tested over a 0–22 cm range of extension and show a significant shift in resonant frequency (e.g., 90 MHz shift for 10 cm stretch). Furthermore, the effect of resonator coil pitch on the extension sensor gain (MHz cm^{-1}) and linear span of the sensor is studied. The repeatability of the sensor gain is confirmed by performing hysteresis cycles. The sensors is coated with polydimethylsiloxane films to protect from electrical shorting in aqueous environments. The coated resonators are placed in a pipe to report flow rates. The sensor with 1 mm coating is found to have the largest gain (0.17 MHz·s mL^{-1}) and linear span (10–100 mL s^{-1}). Thus, flexible resonant sensors with kirigami-inspired patterns can be tuned

via geometric and coating considerations to wirelessly report a large range of extension lengths for potential uses in health monitoring, motion tracking, deformation detection, and soft robotics.

3.2 Introduction

Position and deformation sensing are critical for applications ranging from virtual reality and robotics to motion tracking and health monitoring. Patel et al. (2012); Cotin et al. (1999); Kawamura et al. (2003); Christopher T. Gentile, Michael Wallace, Timothy D. Avalon, Scott Goodman, Richard Fuller (1992) These sensors can be used to provide positional feedback for actuator systems, Gardonio and Elliott (2005); Erhart (1996) estimate the pose and configuration of mechanical or human systems, Lorussi et al. (2004, 2005); Lin et al. (2005) and determine the deformation of a material or structure. Glišić and Simon (2000); Cochrane et al. (2007); Yamada et al. (2011) Recent emphasis on untethered systems requires light, compact, and energy-efficient deformation sensors.Wehner et al. (2016) Additionally, implementation into wearable sensors for human monitoring and soft robotics systems demand significant extents of deformation. Ryu et al. (2015); Park et al. (2015); Nasab et al. (2017); Bartlett et al. (2017); Shepherd et al. (2011); Shan et al. (2013); Mohan et al. (2017) Furthermore, wireless monitoring in these systems can reduce system complexity by eliminating or reducing wiring components and can enable more compliant materials by removing semi-rigid wiring and connection points. Jia et al. (2006); Matsuzaki and Todoroki (2006) Thus, wireless monitoring of deformation with passive elements can provide a path forward for deformation sensing in soft bodies for energy-efficient reporting and control. Butler et al. (2002)

3.3 Background

Wired soft sensors can provide a solution when integrated with wireless communication circuitry (Wi-Fi, Bluetooth, or cellular). Bartlett et al. (2016) These include various designs of stretchable strain sensors, such as dipole, serpentine, spiral, and helical geometries composed of strain-dependent resistive elements such as carbon-impregnated rubbers or compliant microfluidic channels filled with liquid metals. Zhong et al. (2015); Muth et al. (2014); Lee et al. (2014) In each

of these cases, the extra wiring and power consumption of the communication circuitry can limit the utility of untethered applications. Progress is being made on integrating more flexible, wireless sensors for feedback and control of untethered systems. A common solution is imaging, in which motion and position of the device are monitored externally by a camera. Savage et al. (2013); Mautz and Tilch (2011) This works well in structured environments; however, in unstructured environments, where a camera may be blocked or unavailable, this can be a significant challenge. Another approach is the use of resonant sensors to wirelessly report a positional change of soft materials.

Resonant sensors are a long-standing class of passive, wireless sensors that use radio frequency electromagnetic radiation to wirelessly interrogate the scattering parameters of an inductor–capacitor–resistor (LCR) circuit. Bau et al. (2008) The resonant circuit responds to changes in the local dielectric (changes circuit capacitance) which has been exploited for measuring physical parameters such as fluid level, pressures, temperature, and biocatalyst activity. Harpster et al. (2002); Ong et al. (2001); Reuel et al. (2016); Zhai et al. (2010); Yvanoff and Venkataraman (2009); Li and Wang (2015) Flexible LCR sensors have been used to wirelessly measure the strain of compliant materials, such as inductors composed of serpentine copper traces formed as planar Huang et al. (2014) or helical coils. Wu and Hsu (2013a) In the case of the planar coils, the force is set coplanar to the resonator, and the response is predominantly caused by a change in the self capacitance Massarini and Kazimierczuk (1997) (C) of the LCR circuit. In the case of a helical coil, the force is set normal to the spiral plane, the helical distributed length changes, causing a change in inductance (L) which dominates the response. In both cases, the strain causes a geometric change, which causes the resonant frequency of the LCR to shift, however, due to the design of these sensors, they can only report strains of 0–0.3, or in the case of $\approx$ 3 cm structures, a deformation of up to 1 cm. Stretchable antennas can also be used to measure deformation; these are primarily based on liquid metals, but recent works have also shown strategies for metallic deformable antennas. Liu et al. (2019) However, most examples require connected equipment to transmit data, which limits deployment and deformation tracking in dynamic systems. Kubo et al. (2010); So

et al. (2009); Cheng et al. (2009) Recently, an elastomer based-liquid metal wireless strain sensor measured deformations up to 50% strain in the radio-frequency range. Teng et al. (2018)

Emerging techniques in origami and kirigami engineering offer opportunities to create highly tunable materials and interfaces with complex 3D structures, high extensibility, and tunable stiffness. Chan et al. (2017); Hwang and Bartlett (2018); Yan et al. (2017a); Hwang et al. (2018); Yin et al. (2018); Rafsanjani et al. (2018); Dias et al. (2017) Kirigami is the artistic cousin of origami, in which material is cut (rather than folded) to control structure. In terms of strain or deformation monitoring, most kirigami approaches have used resistive or capacitive measurements, requiring a tethered connection, Firouzeh and Paik (2015); Baldwin and Meng (2017); Sun et al. (2018) or have used tethered antennas. Yan et al. (2017b) Wireless kirigami and origami antennas have been demonstrated where the resonant frequency can be tuned based on the extent of folding or deformation. Liu et al. (2014); Yao et al. (2014b); Fu et al. (2018) However, these demonstrations stop short of exploiting such structures to report the extension length via the resonant scattering parameters of the kirigami antenna. Moreover, these are fabricated to have resonant frequencies suitable for telecommunication (GHz) and not lower frequencies for penetration through water and other biologic media (kHz–MHz range). Yao et al. (2014a); Liu et al. (2015)

3.4 Approach

We present a passive resonant sensor that can be engineered into an extensional sensor with a specific gain and dynamic range based on the pattern of kirigami cuts. The kirigami approach allows this new class of LCR sensors to report much larger deformations normal to their surface ($> 10x$ sensor thickness) than previous, encapsulated helical structures. Wu and Hsu (2013b) In this work, planar Archimedean copper traces are patterned on a flexible substrate and cut to allow deformation normal to the planar surface, thus exploiting both changes in inductance and self-capacitance. Moreover, we show how the resonator can be coated to protect from an aqueous environment and the effect these coatings have on the sensor gain and dynamic range. Finally, we

demonstrate the extensional sensor in a closed system, in this case monitoring the volumetric flow rate of water in a closed pipe (a wireless deflection vane).

3.5 Experimental

Fabrication of Resonator for Stretching Test: A circular Archimedean spiral was selected as the pattern for the resonant sensors as it is common, well-characterized in literature, Mohan et al. (1999) and has a geometry applicable for the intended closed system application (pipe with round cross-section). Archimedean spiral resonant traces having an inner diameter of 2 mm, an outer diameter of 54 mm, and varying pitch sizes in the range of 2–5 mm were designed using Rhino 5 software (Figure 1a). The main reason for choosing the above-mentioned dimensions was to keep the resonant frequency of the coated and embedded kirigami sensors below the microwave frequency to achieve a larger penetration depth in water. The cut trace was patterned as a spiral shape having the same pitch size as the resonator and the inner diameter was modified so that the cut trace would be in the middle of the resonator trace. The resonator trace was patterned on Pyralux sheet, which is a thin copper layer (35 μm) on polyimide (25 μm), using an X–Y Plotter and an indelible marker (Figure 1b). The Pyralux was then etched in order to remove the unmasked copper using a traditional etchant solution consisting of the 2-1 volumetric ratio of hydrogen peroxide (H_2O_2) and hydrochloric acid (HCl). As the final step for the resonator preparation, the samples were washed with acetone to release the mask. The cut pattern was then created on the resonator sample using a CO_2 laser cutter so that an onion ring-shaped kirigami-based resonant sensor could be fabricated.

Stretching Test Measurement: The kirigami sensor was wirelessly coupled with a reader antenna consisting of two copper loops having a similar diameter of 54 mm and positioned facing toward each other at a 24 cm distance. The reader antenna was connected to a VNA for monitoring the scattering parameters matrix (S-parameters) of the sensor by capturing the phase and the magnitude of the forward transmission (S_{21}) response between 100–500 MHz. A measurement without sensor was first taken to serve as a control, where the subsequent data would be subtracted by that control. The sensor was placed at one end of the copper loop and the center of the sensor was taped to a

wooden rod. The sensor was stretched by moving the wooden rod toward the other copper loop. The measurement was taken for every 1 cm movement of the wooden rod until it reached the copper loop at the other end. Then, measurement was taken for every 1 cm of the wooden rod moving backward to its original position. This cyclic experiment was repeated for three times.

Fabrication of Coated Resonators: Spiral resonant traces with no inner diameter and an outer diameter of 42.5 mm were used to fit inside the pipe. The traces were etched using the same approach as described above. After etching, the sensor was placed on an acrylic plate within a mold of set casting thicknesses (0.5, 1.0, and 2.0 mm) and then subjected to oxygen plasma treatment at medium power and 750 mTorr for 5 min to improve bonding application (PDC-001; Harrick Plasma). A batch of PDMS elastomer (Sylgard 184 with a 10:1 oligomer-to-curing agent ratio; Dow Corning) was cast in the mold and cured at 80 $^{\circ}C$ for 4 h. The heights of the cured films were measured in five places and found to have final heights of 0.47 ($\pm$ 0.1), 0.74 ($\pm$ 0.11), and 1.63 ($\pm$ 0.92) mm (95 % confidence intervals). The sealed sample was then laser machined (Epilog Laser Fusion M2, 75 watts) in the spiral pattern

Resonator Response Measurements under a Flowing System: In this experimental setup, the two copper wire loops were wrapped around a transparent PVC pipe having an inner diameter of 5.08 cm, an outer diameter of 6.03 cm, and a length of 30.5 cm. The distance between the copper loops was 10 cm. With the pipe positioned vertically, the center of the sensor is fixed at the same height as the upper copper loop. A minimal cross-shaped structure made by cellophane tape was connected to the center of the sensor and adhered to the pipe wall. This structure helped to fix the sensor in the middle of the pipe. Fittings were attached to both ends of the pipe and connected to two tubes: 1) a water supply tube at top and 2) drain tube at the bottom. As the direction of water flow in the pipe is parallel to gravity, the system was first filled with water prior to initializing a flow rate to prevent the presence of an air gap within the system. The water flow rate was then tuned by controlling the globe valve of water supply. The water flow rate was determined by measuring the amount of time for the water outlet flow to fill up a 500 mL measuring cylinder. Same VNA device as above was used to read the transmission response (10–500 MHz) for every flow rate tuned. The

experiment was started with a small flow rate, slowly increased, then decreased, for three cycles, where 5–7 responses were recorded in each tuning direction.

3.6 Results and Discussion

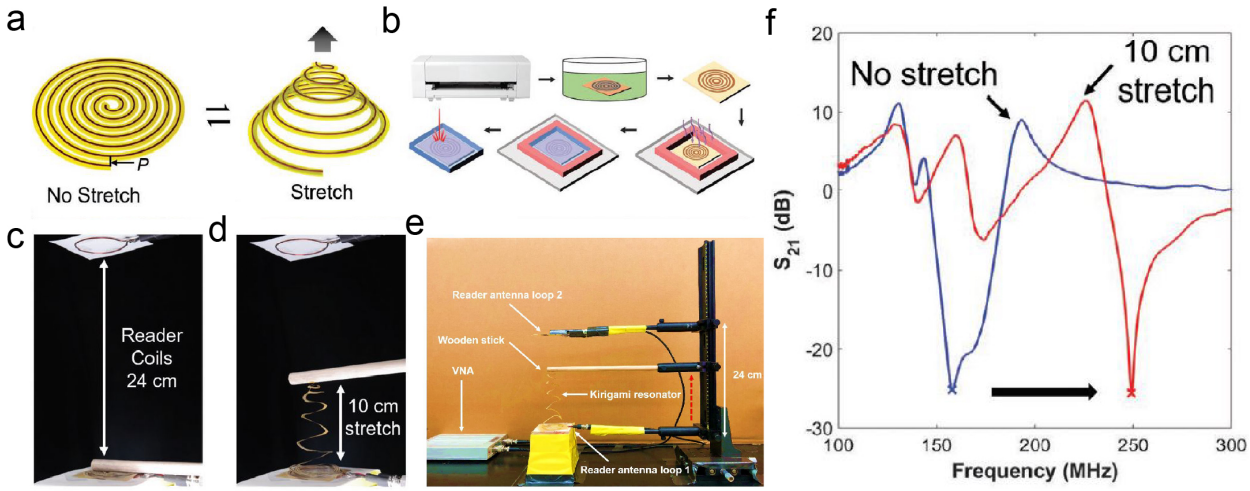

Figure 3.1 a) Design of a kirigami deformation sensor based on an Archimedean spiral at rest and extended; the pitch (P) is the spacing between the resonant traces. b) The fabrication process of the kirigami resonator which includes patterning the resonator trace, etching, releasing mask, coating, and laser cutting. c) The vertical extension test setup with a 3 mm pitch, 5 mm inner diameter, and 54 mm outer diameter resonator at rest (no extension) and d) with 10 cm extension. e) The experimental setup for the stretching test. The red arrow in the figure represents the direction of the sensor extension. f) The S_{21} magnitude response from the sensor in (c,d) depicting the signal minimum used to specify the resonant frequency (marked with "x").

Resonators with fixed outer and inner diameters and varying coil pitch sizes (Figure 3.1a) were fabricated (Figure 3.1b) from etched copper-coated polyimide (Pyralux) as reported before with the additional steps of coating the resonator with a hydrophobic polymer and laser cutting to release the kirigami coil (see Experimental Section). Charkhabi et al. (2018) Pitch (P) is defined as the spacing between the inductive coil lines and the cut is made in the center of the lines (at P/2). These resonators were interrogated by stretching vertically in a 24 cm distance between two reader

antenna loops (3.1c, d, e) which were connected to a benchtop vector network analyzer (VNA). For each sensor, the magnitude of the transmission signal (S_{21}) was monitored over a frequency range of 1–300 MHz. By comparing the resonator's S_{21} magnitude from the rest position to an extended state, it was observed that stretching the sensor causes a significant change in the S_{21} response (Figure 3.1e). This is attributed to a change in the coil's self-capacitance and inductance that is observable in the read range of the interrogating antenna, as described below. The S_{21} response was simplified by tracking the resonant frequency defined as the minimum of the sigmoidal S_{21} feature (160 and 250 MHz in Figure 3.1f), as done in other LCR works. Huang et al. (2014)

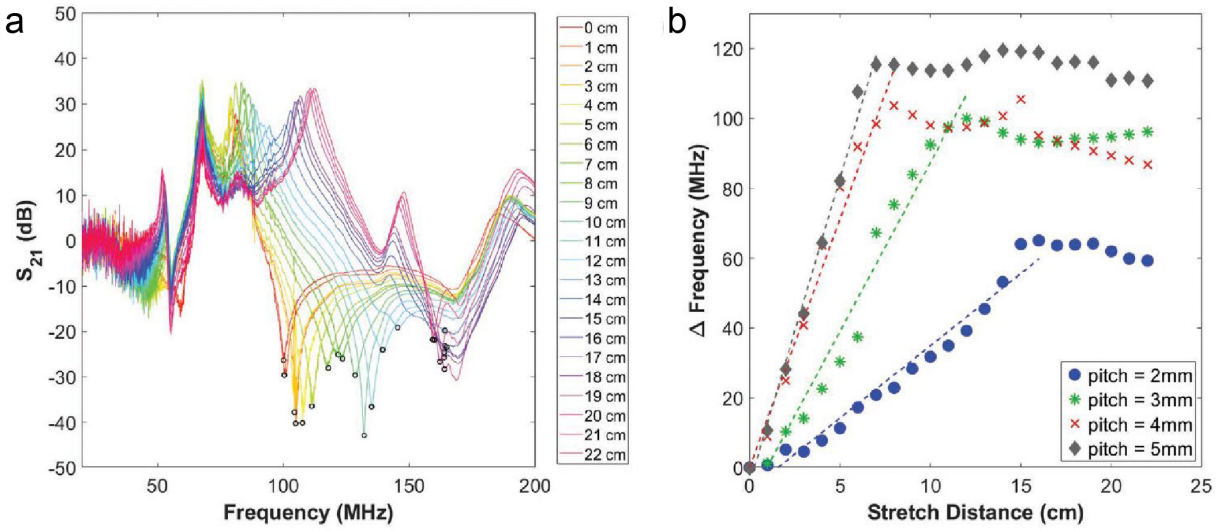

Figure 3.2 a) Kirigami resonant sensor response found from the minima of resonant frequency peaks (circle points) in the transmission magnitude (S_{21} (dB)) response, scanned over the 0–200 MHz frequency range; data shown here for the 2 mm pitch sensor extended from 0–22 cm. b) Resonant frequency response to different stretch distances for kirigami resonators with varying pitch sizes.

The kirigami resonant sensor response was observed over a wide range of stretch distances (0–22 cm at 1 cm intervals) to determine the linearity of sensor response. A linear increase in the resonant frequency was observed as the sensor was stretched (Figure 3.2) up to a specified length; then the resonant frequency sharply remained constant. The proposed mechanism of this response is a change in both the circuit self-capacitance and inductance. When the kirigami LCR resonator is at

rest, the self-capacitance is dictated by the coil to coil spacing. Massarini and Kazimierczuk (1997) When the resonator is pulled out of plane this spacing is increased, and the capacitance decreases much like the spacing of a parallel plate capacitor (Equation (3.1)) where C is the capacitance, ϵ_0 is the permittivity of free space (8.854×10^{-12} Fm^{-1}), ϵ_r is the relative permittivity of the material, A is the capacitive area, and d is the capacitor plate displacement. Bao et al. (2016) Additionally, when the resonator with N number of turns is pulled out of plane it resembles a helical coil, where the inductance (L) is defined by (Equation (3.2)) in which K is the correction factor, l is the axial distributed length, A is the cross-sectional area, and μr and μ0 represent the relative permeability and the permeability of free space, respectively. Thus as the resonator is extended, the length of the coil increases, and the inductance decreases. Since the resonant frequency has an inverse relationship with the capacitance and inductance (Equation (3.3)) where L is the inductance and C is the capacitance), Shen et al. (1977) the resonant frequency would increase by extending the resonant sensor. We observe the sharp leveling off of the sensor response (Figure 3.2b) at the point where all the resonator rings have been lifted off the surface near the interrogating reader antenna. In all geometries tested, the sensor will continue to extend, but the coils begin to warp and the sensor begins to approach a more linear wire geometry, as described below

$$C = \frac{\epsilon_0 \epsilon_r A}{d} \tag{3.1}$$

$$L = K \mu_t \mu_0 \frac{N^2 A}{l} \tag{3.2}$$

$$Resonant Frequency = \frac{1}{2\pi\sqrt{LC}} \tag{3.3}$$

This extension test was repeated for kirigami resonators with different pitches of 3, 4, and 5 mm (Figure 3.2b). In order to study the effect of the resonator's geometry, we characterize two parameters *i*) the sensor gain, defined as the linear slope of the frequency versus stretch curve, and *ii*) the sensor span, defined as the maximum linear deformation the kirigami resonant sensor can report. The gain and span were both found to vary as a function of the resonator pitch. Again,

Table 3.1 The scattering parameter response of the resonant sensor is heavily dependent on the geometrical properties of the resonator. For the Archimedean spiral resonators used in this study, the length of the resonator was controlled by the pitch size since the inner and outer diameters of the spirals were kept constant for different designs. As the pitch size increase, the length of the resonator decreases.

D_i **(mm)**	D_0 **(mm)**	P (mm)	L (mm)
2	54	2	1144
2	54	3	763
2	54	4	573
2	54	5	459

the plateau of the resonant frequency (sensor span) is attributed to the warping and twisting of the kirigami resonant sensor out of the plane of the readers after a certain stretch distance. At this threshold, an increase in extension causes the sensor to twist and elongate, changing from a parallel helical coil to an extended wire perpendicular to the reader loops. This change in deformation pattern, from increasing the coil–coil spacing and helical coil distributed length to a change in perpendicular wire length, would describe this phenomenon. The aforementioned change in capacitance and inductance would no longer be dominant during the wire extension phase and the resonant frequency would remain constant. At this point, the circuit begins to approximate a linear antenna, where the resonant frequency is dictated by the length of conductor alone. The sensor span decreases as the pitch size increases. This observation is attributed to the length of the resonator; a smaller pitch corresponds to an inductor-capacitor (LC) sensor with larger length (Table 3.1). A longer resonator length allows the coils to stay coplanar for a longer extension length, thus increasing the span of the sensor; however, this also reduces the sensor gain.

To check the reversibility of the sensors, we performed hysteresis experiments in which each sensor was stretched and released three times and the gains were calculated during extension and relaxation (Figure 3.5a). The extent to which the sensor was stretched was modified based on the pitch size to make sure that the response remains in the linear portion of the frequency response (i.e., within the sensor span). Each sensor geometry exhibited a small standard deviation of the gain (Figure 3.5b). Also, the gain increases linearly with the pitch size of the resonator (equation

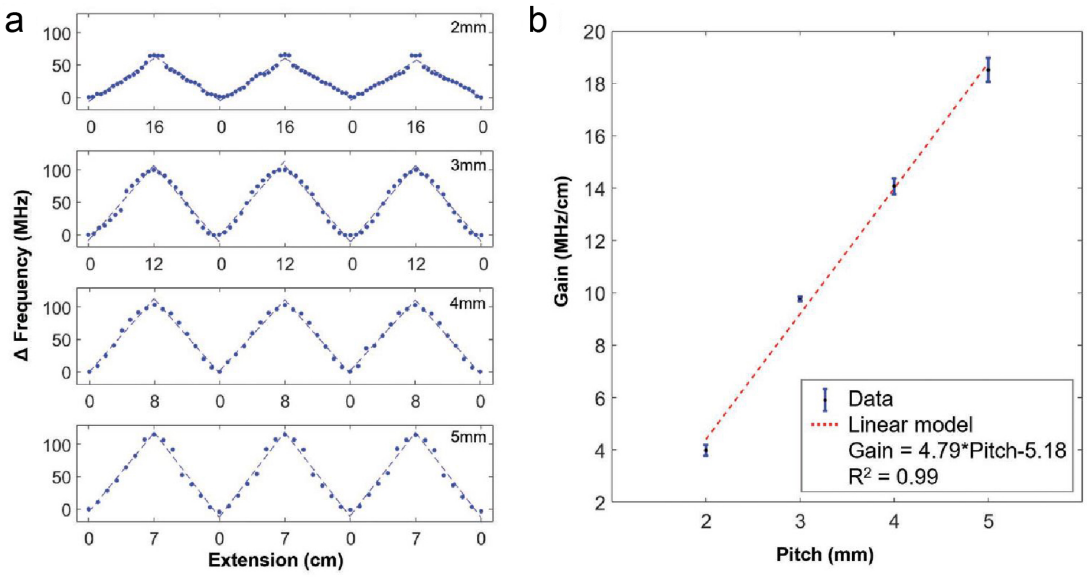

Figure 3.3 a) Kirigami resonant sensor response in a three-cycle hysteresis experiment to determine the consistency of sensor gain (dashed line fit) for different sensor pitch sizes. b) Gains reported for different pitch sizes and the model (dotted line) showing a linear dependence of gain on pitch size. Error bars refer to one standard deviation for n = 6 gains.

insert in Figure 3.5b). As the pitch size increases, the length of the resonator spiral decreases and thus a larger amount of the spiral is pulled out of the interrogation range of the bottom reader coil when extended, thus causing a more dramatic shift in resonant frequency. The linear model fit to the gain versus pitch data has a high coefficient of determination (R^2) at 0.99, thus demonstrating the ability to choose sensor gain based on kirigami resonator pitch size. Moreover, we cycled the 5 mm pitch resonator to 96 cycles to approximate a sensor that undergoes repetitive extensions (Figure 3.4). In this case we found the sensor gain to remain constant, at 14.17 ± 0.20, 14.12 ± 0.10, 14.24 ± 0.14 MHz cm^{-1}, for 1–10, 51–53, and 94–96 cycles respectively (95 % confidence intervals).

The next step to embedding these sensors in actual systems is to protect the conductive surface from shorting, especially in water-based applications. Thus, the sensors were coated with polydimethylsiloxane (PDMS) to insulate the LCR resonator from the external environment. For this purpose, the resonator with P = 5 mm was chosen as the test candidate since it has the steepest

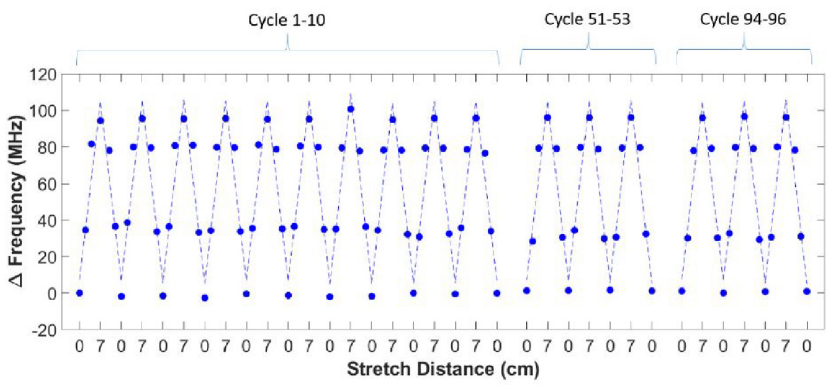

Figure 3.4 96 hysteresis cycle performed on a 5 mm pitch kirigami sensor which was stretched up to 7 cm. The scattering parameter data was captured for displacements of 0, 2, 4, and 7 cm in cycles 1-10, 51-53, and 94-96.

gain (e.g., most responsive). The resonators were coated with varying thicknesses (0.5, 1, and 2 mm cast height, actual height after curing reported in methods) of PDMS by casting the elastomer on the sensor placed within a defined mold. To determine the effect of coating thickness on the sensor gain, three extension hysteresis cycle tests were performed on each resonator in air and the changes in the resonant frequency were measured (Figure 3.5a). The sensor gain was calculated based on each extension and retraction trend (six times in total for each sensor) and was compared for different coating thicknesses (Figure 3.5b). The maximum extension was kept constant at 7 cm for each sensor.

We first observed that starting resonant frequencies were lower for all coated sensors, which we attribute to the altered die- lectric environment. The relative permittivity for air and PDMS is 1 and 2.5 respectively at room temperature which results in a different frequency response window (Figure 3.6). Next, we observed a seemingly discontinuous trend in sensor gain as the coating thickness increases (Figure 3.5b). The uncoated sensor exhibits the highest gain, the minimally-coated sensor (0.5 mm) gain is essentially halved, and then the sensor gains increase as the coating thickness is increased. As described above the sensor response is attributed to geometric changes, but in this case, the coil geometry is the same between all sensors; thus the coating must also have

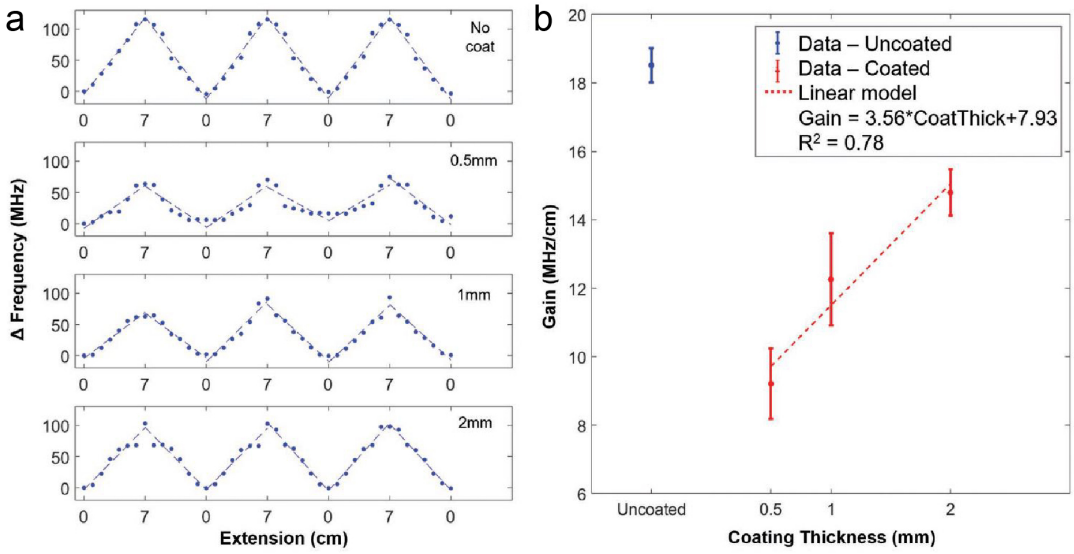

Figure 3.5 a) PDMS-coated, kirigami resonant sensor response to three hysteresis cycles at 0, 0.5, 1, and 2 mm cast thicknesses of PDMS on a 5 mm pitch sensor showing consistent gains in air (dashed line fit). b) Measured gains for the coated sensors with error bars showing one standard deviation for n = 6 gains. Linear model (dashed line) shows a linear relation of gain to coating thickness for 0.5–2 mm coating thickness.

an effect on the manner in which the coil unfolds and extends. Upon closer inspection of stretching footage, we observe that the uncoated coil has very little mass and the polyimide substrate is sufficiently rigid to maintain a regular, helical coil structure. However, the minimal coating adds mass to the coil and due to the large coil compliance, less of the coil length extends from the surface. As the encapsulant coating increases, the coil rigidity increases more rapidly than the added mass and the coil deforms in a manner more similar to the uncoated helical coil. Additionally, we observe an increased variance in the coated resonator gains as compared to the uncoated resonators. This is likely due to the inconsistencies caused by PDMS coating such as stochastic stick–slip phenomena as the PDMS layers rub against each other during extension, which could be reduced in the future, be increasing the cut width.

To determine the applicability of these sensors in a closed system, we utilize PDMS-coated resonant sensors to wirelessly measure the flow rate of liquid in a closed pipe. The sensor was

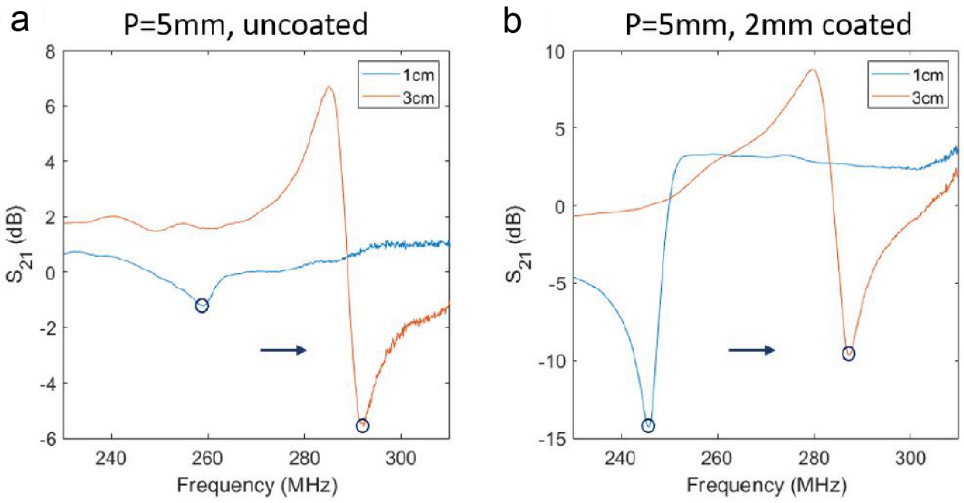

Figure 3.6 a) the S_{21} profile of uncoated 5mm pitch resonator for 1 and 3 cm extension. b) the S_{21} profile for 2mm PDMS-coated 5mm pitch resonator for 1 and 3 cm extension.

placed in a 6 cm diameter polyvinyl chloride (PVC) pipe (transparent for visual confirmation of extension) oriented vertically (such that gravity pulls down on the sensor) and we measured the effect of flow rate on sensor response (Figure 3.7a). The response was observed using two reader antennas looped externally around the pipe at a displacement of 10 cm and connected to the VNA. The center of the resonator was fixed parallel to the top reader loop while the rest of the coil was free to extend or retract with the water flow. The pipe was initially filled with water and flow rates in the range of 0–100 mL s^{-1} were added via a manual control valve.

As anticipated, increasing the water flow rate increased the resonator's extension length which subsequently increased the resonant frequency. A thicker PDMS coating results in a higher sensor stiffness and decreases the extent to which the kirigami resonator stretches for a given flow rate (Figure 3.7b). The change in resonant frequency as a function of flow rate was also recorded for different coating thicknesses (Figure 3.7c). The range of frequency shifts is significantly lower in water when compared to the same resonator in air. We attribute this to the dielectric effect of water ($\epsilon_r \approx 80$ at 20 °C) which shifts the resonant frequency from 240–370 MHz to 85–100 MHz (Figure 3.8). The res- onant frequency is dominated by this water effect and thus the effect of

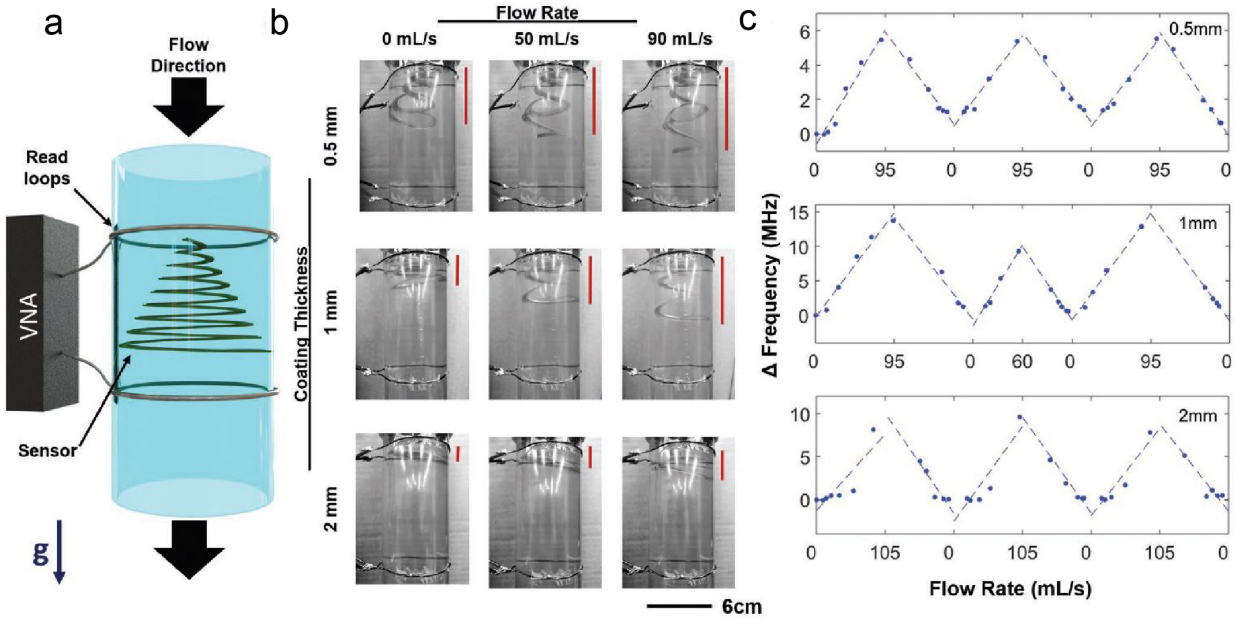

Figure 3.7 a) Schematic of a kirigami resonant sensor reporting the flow rate of water in a closed pipe. b) Images of the sensor stretching caused by water flow through a clear pipe. c) Three cycle hysteresis experiment to observe changes in the resonant frequency based on the flow rate and dependence on coating thickness. Linear gain model shown with dashed lines.

extension is less pronounced on these submerged sensors. Also, in the pipe, the kirigami resonator at no flow rate is not flat (as it is in the resting condition measured in air); thus, the effect of extension due to flow rate would again be less than that observed in air. From the hysteresis plots of the kirigami resonant sensors in a flowing pipe (Figure 3.7c), we observe that the flow sensor gain (change in frequency response divided by the change in flow rate) was not linear with flow rate (as was observed with uniaxial extension).

In Figure 3.9, all the data is presented together, and we clearly observe a threshold flow rate (Q breakthrough, or QBT) before a linear response is again observed. We attribute the breakthrough flow rate to either the friction between adjacent coils caused by the coating or a nonlinear, force–displacement response of the kirigami. This threshold flow rate increases as the coating thickness increases. A higher variation in the gain was observed for thicker coatings,

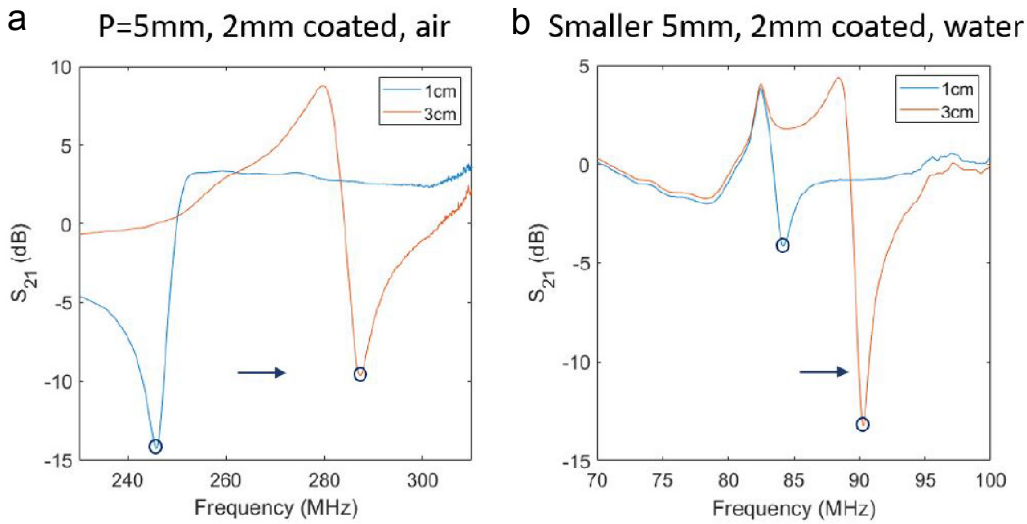

Figure 3.8 S_{21} profile of the resonator with 5mm pitch size and 2mm PDMS coating for 1 and 3cm extensions when a) the resonator is in the air. and b) the resonator is placed in PVC pipe filled with water.

attributed to the stick–slip phenomenon as before. Thicker coatings increase the gain, but if too much is added, it increases the requisite breakthrough flow rate, which would not allow for reporting lower flow rates. From this panel of sensors, the 1 mm coating is optimal since its gain is relatively high and the QBT is low; however, for a system with low flow rates (below 10 mL s^{-1}), the 0.5 mm coating is suggested since it has no observed breakthrough flow rate. The breakthrough limit is not observed in the preceding air extension experiments as those were conducted at specified extension lengths and do not indicate the force required to reach that extension.

3.7 Conclusion

Here we demonstrate the design, fabrication, characterization, and application of kirigami resonant sensors for wireless reporting of extension and retraction in closed environments. The sensor response was monitored wirelessly using a vector network analyzer, observing the changes in reso-

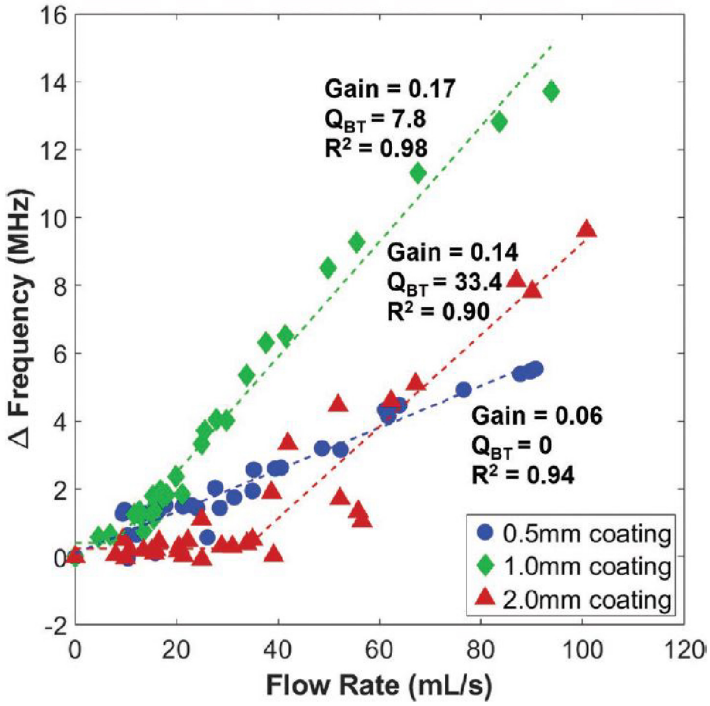

Figure 3.9 The effect of water flow rate on the changes in resonant frequency for 5 mm pitch resonators with 0.5, 1, and 2 mm cast thickness of PDMS coating affixed in a 6 cm diameter pipe. The data were fit with a linear gain with an additional parameter of a breakthrough flow rate. Reported flow sensor gains, breakthrough flow rate, and model coefficient of determination for each coating thickness are presented on the plot. The units for gain and QBT are MHz s mL^{-1} and mL s^{-1}, respectively

nant frequency in the transmission scattering parameter magnitude (S_{21}). Unlike many previously reported resonant deformation sensors, which usually work in millimeter extension ranges, the linearity of this kirigami-inspired resonant sensor can be as high as 16 cm. Furthermore, it was shown that by coating the resonator with PDMS film, the sensor can be applied in both air and aqueous systems. This was demonstrated by wirelessly measuring the flow rate of water in a closed piping system. The kirigami resonator gain exhibits low variability in hysteresis experiments and can be controlled based on pitch size and coating thickness. This portends to their use as reliable and tunable sensors. We anticipate that this type of deformation sensor can be utilized in a variety of applications such as wearable biomonitoring and untethered robotics, where low power, wireless

sensing combined with high extensibility can enable monitoring and control of future untethered systems.

3.8 References

Baldwin, A. and Meng, E. (2017). a Kirigami-Based Parylene C Stretch Sensor. pages 227–230.

Bao, W., Mondal, A. K., Xu, J., Wang, C., Su, D., and Wang, G. (2016). 3D hybrid–porous carbon derived from carbonization of metal organic frameworks for high performance supercapacitors. *Journal of Power Sources*, 325:286–291.

Bartlett, M. D., Kazem, N., Powell-Palm, M. J., Huang, X., Sun, W., Malen, J. A., and Majidi, C. (2017). High thermal conductivity in soft elastomers with elongated liquid metal inclusions. *Proceedings of the National Academy of Sciences of the United States of America*, 114(9):2143–2148.

Bartlett, M. D., Markvicka, E. J., and Majidi, C. (2016). Rapid Fabrication of Soft, Multilayered Electronics for Wearable Biomonitoring. *Advanced Functional Materials*, 26(46):8496–8504.

Bau, H., DeRooij, N. F., and Kloeck, B. (2008). *Sensors, Mechanical Sensors*. Sensors. John Wiley & Sons.

Butler, J. C., Vigliotti, A. J., Verdi, F. W., and Walsh, S. M. (2002). Wireless, passive, resonant-circuit, inductively coupled, inductive strain sensor. *Sensors and Actuators, A: Physical*, 102(1-2):61–66.

Chan, Y. H., Tse, Z., and Ren, H. (2017). Design evolution and pilot study for a kirigami-inspired flexible and soft anthropomorphic robotic hand. In *18th International Conference on Advanced Robotics, ICAR 2017, Hong Kong, China, July 10-12, 2017*, pages 432–437.

Charkhabi, S., Beierle, A. M., McDaniel, M. D., and Reuel, N. F. (2018). Resonant Sensors for Low-Cost, Contact-Free Measurement of Hydrolytic Enzyme Activity in Closed Systems. *ACS Sensors*, 3(8):1489–1498.

Cheng, S., Wu, Z., Hjort, K., Rydberg, A., and Hallbjörner, P. (2009). Foldable and Stretchable Liquid Metal Planar Inverted Cone Antenna OGIR II View project MEMS terahertz systems View project Foldable and Stretchable Liquid Metal Planar Inverted Cone Antenna. *Ieee Transactions on Antennas and Propagation*, 57(12):3765–3771.

Christopher T. Gentile, Michael Wallace, Timothy D. Avalon, Scott Goodman, Richard Fuller, T. H. (1992). Angular Displacement Sensors.

Cochrane, C., Koncar, V., Lewandowski, M., and Dufour, C. (2007). Design and Development of a Flexible Strain Sensor for Textile Structures Based on a Conductive Polymer Composite.

Cotin, S., Delingette, H., and Ayache, N. (1999). Real-time elastic deformations of soft tissues for surgery simulation. *IEEE Transactions on Visualization and Computer Graphics*, 5(1):62–73.

Dias, M. A., McCarron, M. P., Rayneau-Kirkhope, D., Hanakata, P. Z., Campbell, D. K., Park, H. S., and Holmes, D. P. (2017). Kirigami Actuators. *Soft Matter*.

Erhart, T. A. (1996). LINEAR ACTUATOR WITH FEEDBACK POSITION SENSORDEVICE.

Firouzeh, A. and Paik, J. (2015). The Design and Modeling of a Novel Resistive Stretch Sensor with Tunable Sensitivity. *IEEE Sensors Journal*, 15(11):6390–6398.

Fu, H., Nan, K., Bai, W., Huang, W., Bai, K., Lu, L., Zhou, C., Liu, Y., Liu, F., Wang, J., Han, M., Yan, Z., Luan, H., Zhang, Y., Zhang, Y., Zhao, J., Cheng, X., Li, M., Lee, J. W., Liu, Y., Fang, D., Li, X., Huang, Y., Zhang, Y., and Rogers, J. A. (2018). Morphable 3D mesostructures and microelectronic devices by multistable buckling mechanics. *Nature Materials*, 17(3):268–276.

Gardonio, P. and Elliott, S. J. (2005). Modal response of a beam with a sensor–actuator pair for the implementation of velocity feedback control. *Journal of Sound and Vibration*, 284(1):1–22.

Glišić, B. and Simon, N. (2000). Monitoring of concrete at very early age using stiff SOFO sensor. *Cement and Concrete Composites*, 22(2):115–119.

Harpster, T. J., Stark, B., and Najafi, K. (2002). A passive wireless integrated humidity sensor. *Sensors and Actuators A: Physical*, 95(2):100–107.

Huang, X., Liu, Y., Cheng, H., Shin, W.-J., Fan, J. A., Liu, Z., Lu, C.-J., Kong, G.-W., Chen, K., Patnaik, D., Lee, S.-H., Hage-Ali, S., Huang, Y., and Rogers, J. A. (2014). Materials and Designs for Wireless Epidermal Sensors of Hydration and Strain. *Advanced Functional Materials*, 24(25):3846–3854.

Hwang, D. G. and Bartlett, M. D. (2018). Tunable Mechanical Metamaterials through Hybrid Kirigami Structures. *Scientific Reports*, 8(1):1–8.

Hwang, D. G., Trent, K., and Bartlett, M. D. (2018). Kirigami-Inspired Structures for Smart Adhesion. *ACS Applied Materials and Interfaces*, 10(7):6747–6754.

Jia, Y., Sun, K., Agosto, F. J., and Quiñones, M. T. (2006). Design and characterization of a passive wireless strain sensor. *Measurement Science and Technology*, 17(11):2869–2876.

Kawamura, S., Kanaoka, K., Nakayama, Y., Jeon, J., and Fujimoto, D. (2003). Improvement of passive elements for wearable haptic displays. In *2003 IEEE International Conference on Robotics and Automation (Cat. No.03CH37422)*, volume 1, pages 816–821 vol.1.

Kubo, M., Li, X., Kim, C., Hashimoto, M., Wiley, B. J., Ham, D., and Whitesides, G. M. (2010). Stretchable microfluidic radiofrequency antennas. *Advanced Materials*, 22(25):2749–2752.

Lee, J., Kim, S., Lee, J., Yang, D., Park, B. C., Ryu, S., and Park, I. (2014). A stretchable strain sensor based on a metal nanoparticle thin film for human motion detection. *Nanoscale*, 6(20):11932–11939.

Li, S. and Wang, K. W. (2015). Fluidic origami: A plant-inspired adaptive structure with shape morphing and stiffness tuning. *Smart Materials and Structures*, 24(10).

Lin, P.-C., Komsuoglu, H., and Koditschek, D. E. (2005). A leg configuration measurement system for full-body pose estimates in a hexapod robot. *IEEE Transactions on Robotics*, 21(3):411–422.

Liu, F., Chen, Y., Song, H., Zhang, F., Fan, Z., Liu, Y., Feng, X., Rogers, J. A., Huang, Y., and Zhang, Y. (2019). High Performance, Tunable Electrically Small Antennas through Mechanically Guided 3D Assembly. *Small*, 15(1):1804055.

Liu, X., Yao, S., Cook, B. S., Tentzeris, M. M., and Georgakopoulos, S. V. (2015). An Origami Reconfigurable Axial-Mode Bifilar Helical Antenna. *IEEE Transactions on Antennas and Propagation*, 63(12):5897–5903.

Liu, X., Yao, S., Georgakopoulos, S. V., Cook, B. S., and Tentzeris, M. M. (2014). Reconfigurable helical antenna based on an origami structure for wireless communication system. In *2014 IEEE MTT-S International Microwave Symposium (IMS2014)*, pages 1–4.

Lorussi, F., Rocchia, W., Scilingo, E. P., Tognetti, A., and De Rossi, D. (2004). Wearable, redundant fabric-based sensor arrays for reconstruction of body segment posture. *IEEE Sensors Journal*, 4(6):807–818.

Lorussi, F., Scilingo, E. P., Tesconi, M., Tognetti, A., and Rossi, D. D. (2005). Strain sensing fabric for hand posture and gesture monitoring. *IEEE Transactions on Information Technology in Biomedicine*, 9(3):372–381.

Massarini, A. and Kazimierczuk, M. K. (1997). Self-capacitance of inductors. *IEEE Transactions on Power Electronics*, 12(4):671–676.

Matsuzaki, R. and Todoroki, A. (2006). Passive wireless strain monitoring of actual tire using capacitance–resistance change and multiple spectral features. *Sensors and Actuators A: Physical*, 126(2):277–286.

Mautz, R. and Tilch, S. (2011). Survey of optical indoor positioning systems. In *2011 International Conference on Indoor Positioning and Indoor Navigation*, pages 1–7.

Mohan, A. M. V., Kim, N., Gu, Y., Bandodkar, A. J., You, J.-M., Kumar, R., Kurniawan, J. F., Xu, S., and Wang, J. (2017). Merging of Thin- and Thick-Film Fabrication Technologies: Toward Soft Stretchable "Island–Bridge" Devices. *Advanced Materials Technologies*, 2(4):1600284.

Mohan, S. S., Hershenson, M. d. M., Boyd, S. P., and Lee, T. H. (1999). Simple accurate expressions for planar spiral inductances. *IEEE Journal of Solid-State Circuits*, 34(10):1419–1424.

Muth, J. T., Vogt, D. M., Truby, R. L., Mengüç, Y., Kolesky, D. B., Wood, R. J., and Lewis, J. A. (2014). Embedded 3D Printing of Strain Sensors within Highly Stretchable Elastomers. *Advanced Materials*, 26(36):6307–6312.

Nasab, A. M., Sabzehzar, A., Tatari, M., Majidi, C., and Shan, W. (2017). A Soft Gripper with Rigidity Tunable Elastomer Strips as Ligaments. *Soft Robotics*, 4(4):411–420.

Ong, K. G., Grimes, C. A., Robbins, C. L., and Singh, R. S. (2001). Design and application of a wireless, passive, resonant-circuit environmental monitoring sensor. *Sensors and Actuators A: Physical*, 93(1):33–43.

Park, J. J., Hyun, W. J., Mun, S. C., Park, Y. T., and Park, O. O. (2015). Highly Stretchable and Wearable Graphene Strain Sensors with Controllable Sensitivity for Human Motion Monitoring. *ACS Applied Materials & Interfaces*, 7(11):6317–6324.

Patel, S., Park, H., Bonato, P., Chan, L., and Rodgers, M. (2012). A review of wearable sensors and systems with application in rehabilitation. *Journal of NeuroEngineering and Rehabilitation*, 9(1):21.

Rafsanjani, A., Zhang, Y., Liu, B., Rubinstein, S. M., and Bertoldi, K. (2018). Kirigami skins make a simple soft actuator crawl. *Science Robotics*, 3(15):eaar7555.

Reuel, N. F., McAuliffe, J. C., Becht, G. A., Mehdizadeh, M., Munos, J. W., Wang, R., and Delaney, W. J. (2016). Hydrolytic Enzymes as (Bio)-Logic for Wireless and Chipless Biosensors. *ACS Sensors*, 1(4):348–353.

Ryu, S., Lee, P., Chou, J. B., Xu, R., Zhao, R., Hart, A. J., and Kim, S.-G. (2015). Extremely Elastic Wearable Carbon Nanotube Fiber Strain Sensor for Monitoring of Human Motion. *ACS nano*, 9(6):5929–5936.

Savage, V., Chang, C., and Hartmann, B. (2013). Sauron. In *Proc. 26th Annual ACM Symp. User Interface Software and Technology, ACM*, pages 447–456.

Shan, W., Lu, T., and Majidi, C. (2013). Soft-matter composites with electrically tunable elastic rigidity. *Smart Materials and Structures*, 22(8).

Shen, L., Long, S., Allerding, M., and Walton, M. (1977). Resonant frequency of a circular disc, printed-circuit antenna. *IEEE Transactions on Antennas and Propagation*, 25(4):595–596.

Shepherd, R. F., Ilievski, F., Choi, W., Morin, S. A., Stokes, A. A., Mazzeo, A. D., Chen, X., Wang, M., and Whitesides, G. M. (2011). Multigait soft robot. *Proceedings of the National Academy of Sciences of the United States of America*, 108(51):20400–20403.

So, J. H., Thelen, J., Qusba, A., Hayes, G. J., Lazzi, G., and Dickey, M. D. (2009). Reversibly deformable and mechanically tunable fluidic antennas. *Advanced Functional Materials*, 19(22):3632–3637.

Sun, R., Zhang, B., Yang, L., Zhang, W., Farrow, I., Scarpa, F., and Rossiter, J. (2018). Kirigami stretchable strain sensors with enhanced piezoelectricity induced by topological electrodes. *Applied Physics Letters*, 112(25):1–6.

Teng, L., Pan, K., Nemitz, M. P., Song, R., Hu, Z., and Stokes, A. A. (2018). Soft Radio-Frequency Identification Sensors: Wireless Long-Range Strain Sensors Using Radio-Frequency Identification. *Soft Robotics*, 00(00):1–13.

Wehner, M., Truby, R. L., Fitzgerald, D. J., Mosadegh, B., Whitesides, G. M., Lewis, J. A., and Wood, R. J. (2016). An integrated design and fabrication strategy for entirely soft, autonomous robots. *Nature*, 536(7617):451–455.

Wu, S. Y. and Hsu, W. (2013a). Design and characterization of LC strain sensors with novel inductor for sensitivity enhancement. *Smart Materials and Structures*, 22(10).

Wu, S.-Y. and Hsu, W. (2013b). Design and characterization of LC strain sensors with novel inductor for sensitivity enhancement. *Smart Materials and Structures*, 22(10):105015.

Yamada, T., Hayamizu, Y., Yamamoto, Y., Yomogida, Y., Izadi-Najafabadi, A., Futaba, D. N., and Hata, K. (2011). A stretchable carbon nanotube strain sensor for human-motion detection. *Nature Nanotechnology*, 6(5):296–301.

Yan, Z., Pan, T., Yao, G., Liao, F., Huang, Z., Zhang, H., Gao, M., Zhang, Y., and Lin, Y. (2017a). Highly stretchable and shape-controllable three-dimensional antenna fabricated by "cut-Transfer-Release" method. *Scientific Reports*, 7(October 2016):1–7.

Yan, Z., Pan, T., Yao, G., Liao, F., Huang, Z., Zhang, H., Gao, M., Zhang, Y., and Lin, Y. (2017b). Highly stretchable and shape-controllable three-dimensional antenna fabricated by "Cut-Transfer-Release" method. *Scientific Reports*, 7(1):42227.

Yao, S., Georgakopoulos, S. V., Cook, B., and Tentzeris, M. (2014a). A novel reconfigurable origami accordion antenna. In *2014 IEEE MTT-S International Microwave Symposium (IMS2014)*, pages 1–4.

Yao, S., Liu, X., Georgakopoulos, S. V., and Tentzeris, M. M. (2014b). A novel reconfigurable origami spring antenna. In *2014 IEEE Antennas and Propagation Society International Symposium (APSURSI)*, pages 374–375.

Yin, L., Kumar, R., Karajic, A., Xie, L., You, J.-m., Joshuia, D., Lopez, C. S., Miller, J., and Wang, J. (2018). From All-Printed 2D Patterns to Free-Standing 3D Structures: Controlled Buckling and Selective Bonding. *Advanced Materials Technologies*, 3(5):1800013.

Yvanoff, M. and Venkataraman, J. (2009). A Feasibility Study of Tissue Characterization Using LC Sensors. *IEEE Transactions on Antennas and Propagation*, 57(4):885–893.

Zhai, J., How, T. V., and Hon, B. (2010). Design and modelling of a passive wireless pressure sensor. *CIRP Annals*, 59(1):187–190.

Zhong, J., Zhong, Q., Hu, Q., Wu, N., Li, W., Wang, B., Hu, B., and Zhou, J. (2015). Stretchable Self-Powered Fiber-Based Strain Sensor. *Advanced Functional Materials*, 25(12):1798–1803.

CHAPTER 4. GENERAL CONCLUSIONS

4.1 Kirigami principle as a route to multi-functional materials

This work was focused on understanding the geometric parameters which govern mechanical responses and derivative functional responses in the form of stretchable conductors, magnetoactive actuators, and resonant sensors. Specifically, the design concept that couples two dominant deformation modes of kirigami structures allows for tremendous tunability of stiffness by a factor of $\sim$ 30 and ultimate strain by a factor of $\sim$ 2 in an otherwise inextensible sheet. (Chapter 2) Furthermore, the kirigami geometric structure affects the electronic properties the under deformation. The extent of the deformation modulates the capacitance, the inducatance, and the resonant frequency, which is used for measuring the water flow rate in a closed pipe. (Chapter 3) These contributions lay the fundamental foundations for further studies on a variety of material systems by applying the kirigami principles to guide the development of stretchable electronics, soft robotics, and areas that require spatial tuning of elasticity.

4.2 Outlooks

1. Dynamical Control of Elasticity in Kirigami Structures

    - Instead of using materials with intrinsically static material properties and simply tuning geometric parameters, choosing materials that show dynamic responses under external stimuli (*e.g.,* thermal, chemical, electrical, magnetic) may provide additional functionalities. This could facilitate smart kirigami structure which respond to their environment or specific triggers.

2. Robust Interface Through Stiffness Gradients

    - Biomonitoring through wearable electronics is becoming central to daily human lives to enhance our well-being. Thus, creating robust and safe devices is a key factor to take into account. However, the difference in moduli between rigid electronic components and soft substrates such as casing and human skin causes failure and discomfort. The kirigami principle poses a solution to tune the moduli in materials, so that the syetem may remain functional for a longer period of time with greater comfort.

3. Multi-directional wireless sensing with kirigami materials

    - The degree of freedom (DoF) of kirigami materials can be programmed to respond to external environments. The research on the multi-directional sensing capability using soft, stretchable systems has been limited. Thus, expanding our current work through a deterministic design of kirigami structures for richer mechanical responses may allow for a precise measurement of external signals from environments where complex 3D morphing or flows are expected.

4.3 Contributions and Final Remarks

The following specific contributions were presented throughout this work:

- Showed the synergistic mechanical coupling of two dominant deformation modes of kirigami structures to achieve high tunability of stiffness and ultimate strain through hybrid patterns.

- Provided analytical expressions that quantitatively capture the mechanical response of the hybrid kirigami metamaterials, which can act as design crietria to create kirigami-based materials with controlled mechanical properties.

- Investigated the relationship between the resonant scattering paramters of the kirigami antenna and the extension length.